Cohesive Models of Fatigue Crack Growth and Stress-Corrosion Cracking

Thesis by

Olivier T. Nguyen

Electro-Mechanical Engineer, Université de Liège, Belgique, 1996

MSc Aeronautics, California Institute of Technology, USA, 1998

In Partial Fulfillment of the Requirements

for the Degree of

Doctor of Philosophy

California Institute of Technology

Pasadena, California

2002

(Submitted July 9, 2000)

Acknowledgements

I wish to express my foremost and deepest gratitude to my advisor, Professor Michael Ortiz. His guidance, advice and continuous support during my research proved to be invaluable. His constant enthusiasm and extraordinary insight have inspired me throughout my research.

My gratitude goes to Professor Guruswami Ravichandran for advising me on my research and helping me with the numerous questions I had. I would like also to thank Professor Ares J. Rosakis, Professor Anna Pandolfi and Professor James L. Beck for reviewing my thesis. I am indebted to Professor Emily A. Carter and her students, Emily A. A. Jarvis and R. L. Hayes, for many fruitful discussions and suggestions, as well as for making available to me their research results prior to publication. I am thankful for the Office of Naval Research under the grant N00014-96-1-0068 and the Brown University sub-award 983-21054 under AFOSR grant F49620-99-1-0272 for the financial support they have provided me with.

I would like to acknowledge and thank all the current and former members of the Computational Mechanics Laboratory, in particular: Matt Fago, Marisol Koslowski, Adrian Lew, Dr. Jean-Francois Molinari, Dr. Raul Radovitzky, Dr. Eduardo Repetto, Puruav Thoutireddy and Dr. Chengxiang Yu. They were always available to share many useful ideas which helped me to progress in my research.

I am overwhelmed with gratitude to my parents for their unconditional support during these years and especially to my wife, Jayaseeli, for her love, patience and support.

To my wife Jayaseeli and my family.

Abstract

The aim of this dissertation was to develop models of fatigue crack growth and stress-corrosion cracking by investigating cohesive theories of fracture. These models were integrated in a finite-element framework embedding a contact algorithm and techniques of remeshing and adaptive meshing.

For the fatigue model, we developed a phenomenological cohesive law which exhibits unloading-reloading hysteresis. This model qualitatively predicts fatigue crack growth rates in metals under constant amplitude regime for short and long cracks, as well as growth retardation due to overload. Quantitative predictions were obtained in the case of long cracks.

We developed a chemistry-dependent cohesive law which serves as a basis for the stress-corrosion cracking model. In order to determine this cohesive law, two approaches, based on energy relaxation and the renormalization group, were used for coarse-graining interplanar potentials. We analyzed the cohesive behavior of a large—but finite—number of interatomic planes and found that the macroscopic cohesive law adopts a universal asymptotic form. The resulting stress-corrosion crack growth rates agreed well with those observed experimentally in 'static' fatigue tests given in the literature.

Contents

List of Figures

List of Tables

Chapter 1 Introduction

Fatigue of materials has been the subject of extensive research for more than one hundred and fifty years and is still an area full of great challenges for both fundamental studies and engineering applications. The peculiarity of fatigue failure is that it occurs under the action of some driving force which is much smaller than what is needed for classic (monotonic) failure. In addition, fatigue failure can occur in many different forms and spans a wide range of length scales. In his book "Fatigue of Materials," Suresh [89] identifies at least seven sources of fatigue failure, namely mechanical fatigue, creep-fatigue, thermomechanical fatigue, corrosion fatigue, sliding contact fatigue and rolling contact fatigue. It is therefore difficult to understand it fundamentally and this has a significant detrimental effect on the reliability of practical engineering structures.

The development of a comprehensive computational life-predicting tool capable of handling variable amplitude loading, environmental effects, temperature effects and multi-axial loading situations is one of the most challenging task in engineering fatigue design. The need of increased safety and reliability have made this tool especially important for numerous industrial applications, e.g., structures such as bridges, airplanes, nuclear pressure vessels, drilling rigs, and micro-components such as MEMS.

This thesis is focused on two different fatigue failure mechanisms at the macroscopic length scale: mechanical and corrosion fatigue. The first one results from the fluctuation of externally applied stress, while the latter one results from the presence of a chemically aggressive environment.

The intrinsic multiscale character of fracture predicates that macroscopic models of fracture, e.g., those described by the cohesive theories of fracture, should fully resolve the physical mechanisms of crack formation at finer scales. The use of multiscale models with the explicit resolution of different length scales should provide answers

to this problem. However, such models might prove to be unfeasible or impractical, if for example the range of length scales were too large. An alternative—and maybe more viable—strategy is to derive an effective macroscopic behavior from a proper renormalization of the physical mechanisms at finer scales. The latter alternative is pursued in the second part of this work and serves as a basis for the derivation of the chemistry-dependent cohesive law used in the stress-corrosion cracking model in metals. In the first part of this dissertation, we focus our attention on the mechanical fatigue of metals at the macroscopic length scale.

In Chapter 2, we develop a macroscopic cohesive model for fatigue crack growth. An essential characteristic of the cohesive law is that it exhibits unloading-reloading hysteresis to simulate dissipative mechanisms such as crystallographic slip and frictional interactions between asperities. This feature has the additional important consequence of preventing shakedown and allowing for steady crack growth. The near-tip plastic fields and cohesive zone are resolved explicitly by employing adaptive meshing. The material description accounts for cyclic plasticity through a combination of isotropic and kinematic hardening and it also accounts for finite deformations such as those accompanying the blunting of the crack tip. Crack closure is likewise accounted for explicitly as a contact constraint. Several specific examples demonstrate that such a model is capable of a unified treatment of long cracks under constant-amplitude loading, short cracks, and the effect of overloads without *ad hoc* corrections or tuning.

In Chapter 3, we extend the previous model to account for fatigue initiation. We restrict our attention to a specific material point in the target material from which a fatigue crack could be initiated. The number of cycles to failure for that material point as a function of load parameters is compared with experimental results.

In the second part of this dissertation, starting with Chapter 4, we investigate the macroscopic behavior of cohesive laws in the case of cleavage fracture. Cleavage fracture involves the simple separation of atomic planes. It is therefore governed by interplanar potentials which are amenable to an effective ab-initio characterization. An adequate description of cleavage fracture at the macroscale is contingent on the

integration of interplanar potentials into engineering calculations—thereby requiring full atomistic resolution in the vicinity of the crack tip. However, this approach is often unfeasible or impractical. An alternative strategy, which is pursued in this work, is to parameterize the interplanar potentials on a coarse-grain level and then determine the corresponding macroscopic law. Coarse-graining is achieved by investigating the cooperative behavior of a large number of interatomic planes forming a cohesive layer. Using two methods of investigation based on energy relaxation and renormalization-group transformation, we find that the macroscopic cohesive law in the limit of large—but finite—interatomic planes adopts a universal form which is completely determined by the elastic moduli, lattice constants and surface energies.

In Chapter 5, we investigate the environmental effect on the fatigue behavior of metals. Hydrogen embrittlement is considered to be the main mechanism of damage. The hydrogen concentration in the host metal is governed by a diffusion equation which incorporates localization of hydrogen due to hydrostatic stress. By utilizing a thermodynamic framework developed by Rice and Wang [80], the universal cohesive law of Chapter 4 was modified in order to account for the presence of embrittling species such as hydrogen. The critical energy release rate is generalized to be a decreasing function of the hydrogen concentration. Calculations show that such a model successfully predicts the time to failure of metal sample immersed in an aggressive environment under static loading.

Chapter 2 A Cohesive Model of Fatigue Crack Growth

2.1 Introduction

The work presented in this chapter is concerned with the development and validation of a finite-element model of fatigue crack growth in metals. We will start by defining the finite-element methodology used for such purpose. Next, we introduce a cohesive law which exhibits unloading-loading hysteresis allowing for steady crack growth under cyclic loadings. Finally, we validate our model through various comparisons with experiments.

Fatigue life prediction remains very much an empirical art at present. Following the pioneering work of Paris [71, 70], phenomenological laws relating the amplitude of the applied stress intensity factor, ΔK and the crack growth rate, da/dN, have provided a valuable engineering analysis tool. Indeed, Paris's law successfully describes the experimental data under 'ideal' conditions of small-scale yielding, constant amplitude loading and long cracks [41, 1]. However, when these stringent requirements are not adhered to, Paris's law loses much of its predictive ability. This has prompted a multitude of modifications of Paris's law intended to suit every conceivable departure from the ideal conditions: so-called R effects [25, 95]; threshold limits [44, 19, 50]; closure [22]; variable amplitude loads and overloads [96, 97]; small cracks [24, 23]; and others. The case of short cracks is particularly troublesome as Paris's law-based designs can significantly underestimate their rate of growth [89].

The proliferation of *ad hoc* fatigue laws would appear to suggest that the essential physics of fatigue-crack growth is not completely captured by theories which are based on the stress-intensity factors as the sole crack-tip loading parameters. A possible alternative approach, which is explored in this chapter, is the use of cohesive theories

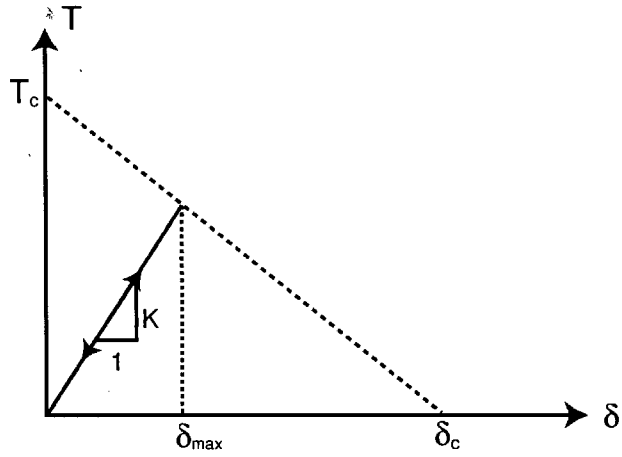

Figure 2.1: Cohesive law with irreversible behavior.

of fracture, in conjunction with the explicit resolution of the near-tip plastic fields and the enforcement of closure as a contact constraint. Cohesive theories regard fracture as a gradual process in which separation between incipient material surfaces is resisted by cohesive tractions. Under monotonic loading, the cohesive tractions eventually reduce to zero upon the attainment of a critical opening displacement. The formation of new surface entails the expenditure of a well-defined energy per unit area, known variously as specific fracture energy or critical energy release rate.

A number of cohesive models have been proposed–and successfully applied–to date for purposes of describing monotonic fracture processes [54, 55, 57, 65, 61, 11, 91, 16, 62, 68, 77]. In some models, unloading from–and subsequent reloading towards–the monotonic envelope is taken to be linear, e. g., towards the origin, and elastic or nondissipative [11, 12], Fig. 2.1. As it turns out, however, such models cannot be applied to the direct cycle-by-cycle simulation of fatigue crack growth. Thus, our simulations reveal that a crack subjected to constant-amplitude cyclic loading, and obeying a cohesive law with elastic unloading, tends to *shake down*, i. e., after the passage of a small number of cycles all material points, including those points on the cohesive zone, undergo an elastic cycle of deformation, and the crack arrests. The centerpiece of the present approach is an irreversible cohesive law with unloading-reloading hysteresis. The inclusion of unloading-reloading hysteresis into the cohesive law is intended

to simulate simply dissipative mechanisms such as crystallographic slip [3, 40] and frictional interactions between asperities [30]. Consideration of unloading-reloading hysteresis proves critical in one additional respect: the attainment of an elastic cycle is not possible if the cohesive law exhibits unloading-reloading hysteresis, and the possibility of shakedown–and the attendant spurious crack arrest–is eliminated altogether. Frictional laws exhibiting unloading-reloading hysteresis have been applied to the simulation of fatigue in brittle materials [31, 34, 38, 101].

The plastic near-tip fields, including the reverse loading that occurs upon unloading, are also known to play an important role in fatigue crack growth [78, 59, 46, 88, 89]. Models based on dislocation pile–ups [7] or 'superdislocations' [3, 40] have been proposed to describe the plastic activity attendant to crack growth. The Dugdale-Barenblatt [4, 21] strip yield model was used by Budiansky and Hutchinson [10] to exhibit qualitatively the effects of closure, thus demonstrating the importance of the plastic wake in fatigue crack growth.

Here, we propose to resolve the near-tip plastic fields and the cohesive zone explicitly by recourse to adaptive meshing. In particular, the plastic dissipation attendant to crack growth is computed explicitly and independently of the cohesive separation processes, and therefore need not be lumped into the crack-growth initiation and propagation criteria. The material description accounts for cyclic plasticity through a combination of isotropic and kinematic hardening; and for finite deformations such as accompany the blunting of the crack tip. Crack closure is likewise accounted for explicitly as a contact constraint.

In the present approach, crack growth results from the delicate interplay between bulk cyclic plasticity, closure, and gradual decohesion at the crack tip. Since the calculations explicitly resolve all plastic fields and cohesive lengths, the approach is free from the restriction of small-scale yielding. This opens the way for a unified treatment of long cracks, short cracks, and fully-yielded configurations. In addition, load-history effects are automatically and naturally accounted for by the path-dependency of plasticity and of the cohesive law. This effectively eliminates the need for *ad hoc* cycle-counting rules under variable-amplitude loading conditions, or for *ad hoc* rules

to account for the èffect of overloads.

This chapter is organized as follows. We begin by setting the basis of the finite element model for fatigue simulation in Section 2.2. The cohesive law is defined in Subsection 2.2.1. Then follows Subsection 2.2.2 on cyclic plasticity. Finally, Subsection 2.2.3 describes the finite element implementation of the model. In Section 2.3, we present the results of validation tests which establish the predictive ability of the model under a variety of conditions of interest. We begin by establishing that the model exhibits Paris-like behavior under ideal conditions of long cracks, small-scale yielding and constant amplitude loading. Finally, we show that the model captures the small-crack effect and the effect of overloads without *ad hoc* corrections or tuning.

2.2 Description of the Model

We have developed a finite element model to simulate the fatigue behavior of a plane strain specimen. The simulation was performed by an implicit integration of the equilibrium equations using a Newton-Raphson algorithm to resolve the non–linear system of equations [14]. The main constituents of the model are described in the next three Subsections, 2.2.1, 2.2.2 and 2.2.3.

2.2.1 A Cohesive Law with Unloading-Reloading Hysteresis

The centerpiece of the present approach is the description of the fracture processes by means of an irreversible cohesive law with unloading-reloading hysteresis. The inclusion of unloading-reloading hysteresis within the cohesive law is intended to account, in some effective and phenomenological sense, for dissipative mechanisms such as frictional interactions between asperities [30] and crystallographic slip [3, 40]. As noted earlier, consideration of loading-unloading hysteresis additionally has the far-reaching effect of preventing shakedown after a few loading cycles and the attendant spurious crack arrest.

We start by considering monotonic loading processes resulting in pure mode I opening of the crack. As the incipient fracture surface opens under the action of the

loads, the opening is resisted by a number of material-dependent mechanisms, such as cohesion at the atomistic scale, bridging ligaments, interlocking of grains, and others [1]. For simplicity, we assume that the resulting cohesive traction T decreases linearly with the opening displacement δ, and eventually reduces to zero upon the attainment of a critical opening displacement δ_c (e. g., [68, 11, 77]); see Fig. 2.1. In addition, separation across a material surface is assumed to commence when a critical stress T_c is reached on the material surface. We note that, prior to the attainment of the critical stress, the opening displacement is zero, i. e., the potential cohesive surface is fully coherent. We shall refer to the relation between T and δ under monotonic opening as the monotonic cohesive envelope. More elaborate monotonic cohesive envelopes than the one just described have been proposed by a number of authors [56, 79, 99], but these extensions will not be pursued here in the interest of simplicity.

The critical stress T_c may variously be identified with the macroscopic cohesive strength or the spall strength of the material. In addition, the area under the monotonic cohesive envelope,

$$G_c = \int_0^{\delta_c} T(\delta) d\delta = \frac{1}{2}\sigma_c \delta_c, \tag{2.1}$$

equals twice the intrinsic fracture energy or critical energy release rate of the material. In general, the macroscopic or measured critical energy-release rate may be greatly in excess of G_c by virtue of the plastic dissipation attendant to crack initiation and growth. In addition, $G_c/2$ may itself be greatly in access of the surface energy owing to dissipative mechanisms occurring on the scale of the cohesive process zone.

For fatigue applications, specification of the monotonic cohesive envelope is not enough and the cohesive behavior of the material under cyclic loading is of primary concern. We shall assume that the process of unloading from–and reloading towards–the monotonic cohesive envelope is hysteretic. For instance, in some materials the cohesive surfaces are rough and contain interlocking asperities or bridging grains [30]. Upon unloading and subsequent reloading, the asperities may rub against each other, and this frictional interaction dissipates energy. In other materials, the crack surface is bridged by plastic ligaments which may undergo reverse yielding upon

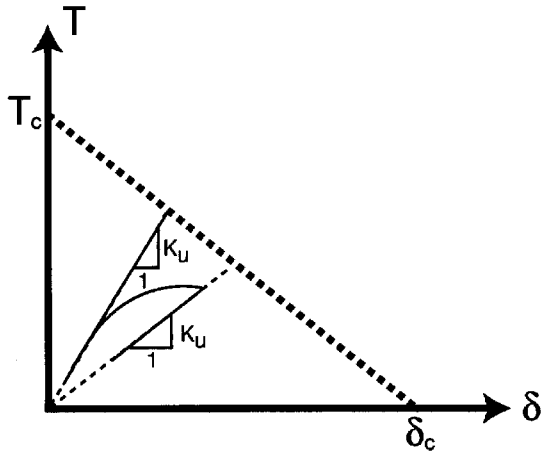

Figure 2.2: Cyclic cohesive law with unloading-reloading hysteresis.

unloading. Reverse yielding upon unloading may also occur when the crack growth is the result of alternating crystallographic slip [3, 40]. In all of these cases, the unloading and reloading of the cohesive surface may be expected to entail a certain amount of dissipation and, therefore, be hysteretic.

Imagine, furthermore, that a cohesive surface is cycled at low amplitude after unloading from the monotonic cohesive envelope. Suppose that the amplitude of the loading cycle is less than the height of the monotonic envelope at the unloading point, Fig. 2.2. We shall assume that the unloading-reloading response degrades with the number of cycles. For instance, repeated rubbing of asperities may result in wear or polishing of the contact surfaces, resulting in a steady weakening of the cohesive response. A class of simple phenomenological models which embody these assumptions is obtained by assuming different incremental stiffnesses depending on whether the cohesive surface opens or closes, i. e.,

$$\dot{T} = \begin{cases} K^- \, \dot{\delta}, & \text{if } \dot{\delta} < 0 \\ K^+ \, \dot{\delta}, & \text{if } \dot{\delta} > 0 \end{cases} \tag{2.2}$$

where K^+ and K^- are the loading and unloading incremental stiffnesses respectively. In addition, we take the stiffnesses $K^{\pm}$ to be internal variables in the spirit of damage theories, and their evolution to be governed by suitable kinetic equations. For

simplicity, we shall assume that unloading always takes place towards the origin of the $T - \delta$ axes, i. e.,

$$K^- = \frac{T_{\max}}{\delta_{\max}} \tag{2.3}$$

where $T_{\max}$ and $\delta_{\max}$ are the traction and opening displacement at the point of load reversal, respectively. In particular, K^- remains constant for as long as crack closure continues. By contrast, the reloading stiffness K^+ is assumed to evolve in accordance with the kinetic relation:

$$\dot{K}^+ = \begin{cases} -K^+ \dot{\delta}/\delta_f, & \text{if } \dot{\delta} > 0 \\ (K^+ - K^-)\, \dot{\delta}/\delta_f, & \text{if } \dot{\delta} < 0 \end{cases} \tag{2.4}$$

where δ_f is a characteristic opening displacement. Evidently, upon unloading, $\dot{\delta} < 0$, K^+ tends to the unloading slope K^-, whereas upon reloading, $\dot{\delta} > 0$, K^+ degrades steadily. Finally, we assume that the cohesive traction cannot exceed the monotonic cohesive envelope. Consequently, when the stress-strain curve intersects the envelope during reloading, it is subsequently bound to remain on the envelope for as long as the loading process ensues.

Evidently, the details of the kinetic equations for the unloading and reloading stiffnesses just described are largely arbitrary, and the resulting model is very much phenomenological in nature. However, some aspects of the model may be regarded as essential and are amenable to experimental validation. Consider, for instance, the following thought experiment. A cohesive surface is imparted a uniform opening displacement $\delta_0 < \delta_c$ and subsequently unloaded. Let K_0^+ be the initial reloading stiffness after the first unloading. The cohesive surface is then cycled between the opening displacements 0 and δ_0. Let K_N^+ be the initial reloading stiffness after N cycles. A straightforward calculation using Eqs. (2.3) and (2.4) then gives

$$K_{N+1}^+ = \lambda\, K_N^+ \tag{2.5}$$

where

$$\lambda = \frac{\delta_f}{\delta_0}(1 - \mathrm{e}^{-\delta_0/\delta_f})^2 + \mathrm{e}^{-2\delta_0/\delta_f} \tag{2.6}$$

is a decay factor. Likewise, we have

$$T_{N+1} = \lambda T_N \tag{2.7}$$

where

$$T_N = K_N^+ \delta_f (1 - \mathrm{e}^{\delta_0/\delta_f}) \tag{2.8}$$

is the traction at the end of the Nth cycle. Iterating the recurrence relations (2.5) and (2.7) gives

$$K_N^+ = \lambda^N K_0^+ \tag{2.9}$$

and

$$T_N = \lambda^N T_0 \tag{2.10}$$

It is clear from these relations that both the initial reloading stiffness and the traction at maximum opening decay exponentially with the number of cycles. In the case of primary interest, $\delta_f \gg \delta_c$, we have

$$\lambda \sim 1 - \frac{\delta_0}{\delta_f} + h.o.t. \tag{2.11}$$

It follows from this expression that, to first order, the model predicts the decay factor λ to decrease linearly with the displacement amplitude of the cycles. In addition, to first order (2.9) and (2.10) reduce to

$$K_N^+ = \mathrm{e}^{-N\delta_0/\delta_f} K_0^+ \tag{2.12}$$

and

$$T_N = \mathrm{e}^{-N\delta_0/\delta_f} T_0 \tag{2.13}$$

and the characteristic opening displacement follows as

$$\delta_f = \frac{\delta_0}{\log(T_N/T_{N+1})} = \frac{\delta_0}{\log(K_N^+/K_{N+1}^+)} \tag{2.14}$$

independently of N. The exponential decay of the maximum traction under constant amplitude displacement cycling of the cohesive law is an essential feature of the model which can be tested experimentally. In addition, equation (2.14) provides a basis for the experimental determination of the parameter δ_f.

Simple methods of extension of models such as just described to account for mixed loading and combined opening and sliding have been discussed elsewhere [12, 62]. An account of issues pertaining to finite kinematics and the requirements of material frame indifference may be found in [62].

2.2.2 Cyclic Plasticity

Cohesive theories of fracture introduce a characteristic length into the description of material behavior. As noted by Camacho and Ortiz [12], for finite element calculations to result in mesh independent results, the cohesive length must be resolved by the mesh. Since, for the class of ductile materials contemplated here, the cohesive zone is often buried deeply within the near-tip plastic zone, the resolution of the cohesive length necessarily results also in the resolution of the plastic zone. One appealing consequence of this resolution is that the plastic fields, and, in particular, the plastic dissipation attendant to the crack opening, are computed explicitly within the model and need not be lumped, in some effective sense, into the description of fracture.

In the simulations reported here we adopt a conventional J_2-flow theory of plasticity with power-law kinematic hardening and rate-sensitivity. A brief account of the model follows for completeness. More comprehensive reviews of these formulations are available in the literature ([20, 15, 89]). We start by formulating the constitutive relations in the framework of small strains or linearized kinematics. In this limit, Hooke's law takes the form

$$\boldsymbol{\sigma} = \mathbf{c}(\boldsymbol{\epsilon} - \boldsymbol{\epsilon}^p) \tag{2.15}$$

where $\boldsymbol{\sigma}$ is the stress tensor, $\mathbf{c}$ are the elastic moduli, which we assume to be isotropic, $\boldsymbol{\epsilon}$ is the strain tensor, and $\boldsymbol{\epsilon}^p$ is the plastic strain tensor. The plastic strain rate is assumed to obey the Prandtl-Reuss flow rule

$$\dot{\boldsymbol{\epsilon}}^p = \dot{\varepsilon}^p \frac{3}{2} \frac{\mathbf{s} - \boldsymbol{B}}{\sigma} \tag{2.16}$$

where ε^p is the effective plastic strain, $\mathbf{s}$ is the stress deviator, $\boldsymbol{B}$ is the back-stress tensor, and

$$\sigma = \left[\frac{3}{2} (\mathbf{s} - \boldsymbol{B}) \cdot (\mathbf{s} - \boldsymbol{B}) \right]^{1/2} \tag{2.17}$$

is the effective Mises stress. The effective plastic strain is assumed to obey a rate-sensitivity power-law of the form

$$\dot{\varepsilon}^p = \dot{\varepsilon}_0^p \left(\frac{\sigma}{\sigma_y} - 1 \right)^m, \quad \sigma \geq \sigma_y \tag{2.18}$$

where $\dot{\varepsilon}_0^p$ is a reference plastic strain rate, m is the rate-sensitivity exponent, and σ_y is the yield stress. We further assume a hardening power-law of the form

$$\sigma_y = \sigma_0 \left(1 + \frac{\varepsilon^p}{\varepsilon_0^p} \right)^{1/n} \tag{2.19}$$

where σ_0 is the initial yield stress, ε_0^p is a reference plastic strain, and n is the hardening exponent. We further assume an equation of evolution for the backstress of the Ziegler form [74, 102]

$$\dot{\boldsymbol{B}} = \dot{\sigma}_y \frac{3}{2} \frac{\mathbf{s} - \boldsymbol{B}}{\sigma} \tag{2.20}$$

In calculations, these equations are discretized in time by the fully-implicit backward-Euler method [63]. In addition, we use the method of extension of Cuitiño and Ortiz [14] in order to extend the material description– and the corresponding update algorithm–into the finite deformation range. Consideration of finite kinematics is required, e. g., near the tip of the crack in order to account for the effect of crack-tip blunting.

2.2.3 Finite Element Implementation

We use six-node isoparametric quadratic elements with three quadrature points per element for the discretization of the domain of analysis. These elements do not lock in the near-incompressible limit and can therefore be used reliably in applications, such as envisioned here, involving volume-preserving large plastic deformations. Cohesive

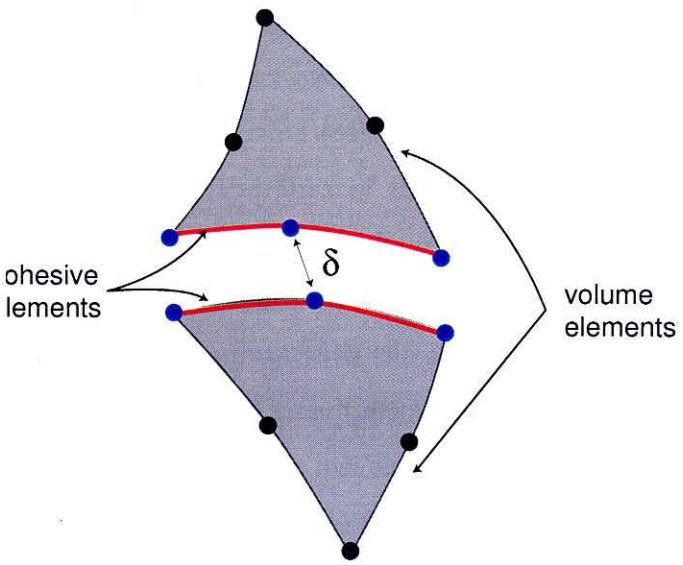

Figure 2.3: Geometry of a six-node cohesive element bridging two six-node triangular elements.

laws such as described earlier, can be conveniently embedded into double-layer–or 'cohesive'–elements [65, 100, 12, 62, 16, 62, 77]. The geometry of the cohesive elements used in calculations, and their adjacency relations to the volume elements they bridge, is shown in Fig. 2.3. These cohesive elements are a two-dimensional specialization of the general class of finite-deformation cohesive elements developed by Ortiz and Pandolfi [62]. The elements consist of two three-node quadratic segments representing the two material surfaces bridged by the cohesive law. The displacement interpolation within each material surface is quadratic. Following Ortiz and Pandolfi [62], all geometrical calculations, including the computation of normals, are carried out on the middle surface of the element, defined as the surface which is equidistant from the material surfaces. The calculations presented subsequently are concerned with straight cracks under pure mode I loading, and, hence, the middle surface simply

coincides with the plane of the crack at all times.

As may be recalled, we assume the cohesive response of material surfaces to be rigid prior to the attainment of the cohesive strength T_c of the material. In the finite-element context this implies that all boundaries between volume elements are initially fully coherent. As the deformation proceeds, cohesive elements are inserted at those element boundaries where the cohesive strength is attained. The subsequent opening of the cohesive surface is governed by the cyclic cohesive law formulated in Section 2.2.1. Upon closure, the contact constraint is enforced through a conventional augmented-Lagrangian contact algorithm [84].

As mentioned earlier, one of the aims of the present approach is the explicit resolution of all the near-tip fields, including the plastic fields, down the scale of the cohesive zone. This confers the calculations a clear *multiscale* character, in that the macroscopic lengthscale, commensurate with the size of the specimen, and selected microscopic lengthscales, are resolved simultaneously. The resulting multiresolution demands of the model may effectively be met with the aid of adaptive meshing.

Evidently, in the vicinity of the cohesive zone, the mesh size must equal a small fraction of the cohesive zone size. The mesh can then be progressively coarsened away from the crack tip. The optimal mesh gradation of the mesh can be deduced from standard interpolation error estimates [76]. For a linear-elastic $K-field$, the optimal mesh-size distribution $h(\mathbf{x})$ is found to go as $r^{3/4}$, where r is the distance to the crack tip. In particular, the optimal mesh size tends to zero as the crack tip is approached.

Based on these considerations we design the mesh near the crack tip to have a $r^{3/4}$ size gradation down to a distances of the order of the cohesive length, below which the element size is held constant at a fraction of the cohesive zone size. In order to keep the problem size within manageable bounds, the full length of the plastic wake left behind by the advancing crack tip is not resolved by the mesh.

Meshes are constructed automatically by first meshing all the edges defining the boundary of the domain of analysis, including the flanks of the crack, at the required nodal density. The geometry of these edges is continuously updated so as to track the

crack advance. The interior meshes are constructed by inserting nodes in a hexagonal lattice arrangement at the target local nodal density. The nodal set is subsequently triangulated by an advancing front method [76]. Examples of meshes used in calculations are shown in Figs. 2.5 and 2.6. The high quality of the meshes in the presence of steep gradients in element size is particularly noteworthy.

The calculations proceed incrementally and the quasistatic equilibrium equations are satisfied implicitly by recourse to a Newton-Raphson iteration. As the crack advances, the near-tip mesh is continuously shifted so as to be centered at the current crack tip at all times. After every remeshing, the displacements, stresses, plastic deformations and effective plastic strains are *transferred* from the old to the new mesh. The transferred fields define the initial conditions for the next incremental step. The details of the transfer operator are given in [64].

2.3 Comparison with Experiment

Next we proceed to assess the predictive ability of the theory in three regimes of interest: fatigue crack growth of long cracks in the Paris regime; fatigue crack growth of short cracks; and the effect of overloads on growth rates in long cracks. It is well-documented experimentally that, for long cracks in many materials subjected to constant-amplitude load cycles, the rate of growth of the crack is proportional to a power of the stress-intensity factor amplitude range [69]. We therefore start by showing that, under the conditions just stated, the theory predicts the requisite Paris behavior. Once this is established, we proceed to investigate the implications of the theory in regimes for which Paris's law is not applicable.

2.3.1 Fatigue Crack Growth of Long Cracks in the Paris Regime

We consider a center-crack panel of aluminum 2024-T351 subject to constant amplitude tensile load cycles, Fig. 2.4. The load is applied uniformly on the edges of the

Young's modulus E	70 GPa
Poisson's ratio ν	0.3
Initial yield stress σ_0	325 MPa
Hardening exponent n	8
Reference plastic strain ε_0^p	0.0002
Rate sensitivity exponent m	100
Reference plastic strain rate $\dot{\varepsilon}_0^p$	$0.08s^{-1}$
Specific cohesive energy G_c	13.8 kJ/m^2
Cohesive strength T_c	800 MPa
Decay displacement δ_f	4 mm

Table 2.1: Aluminum 2024-T3 material parameters used in fatigue calculations.

panel and is cycled between zero and a prescribed amplitude. Owing to the symmetries of the problem, the analysis may be restricted to one quarter of the specimen. The material properties used in the calculations are collected in Table 2.3.1. The value of δ_f has been estimated from archival experimental data [2]. The initial half-

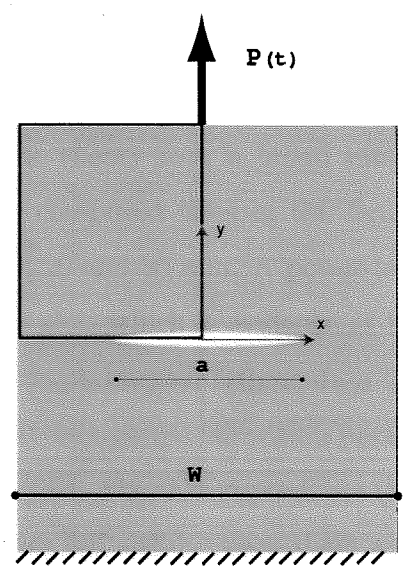

Figure 2.4: Schematic of a center-crack panel test.

crack size a_0 is taken to be 10mm. An overall view of initial mesh used in calculations and a zoom of the near-tip region are shown in Fig. 2.5. In this figure, the centerline of the specimen is on the right.

During the first load cycle, the stresses rise sharply at the crack tip and the crack grows abruptly. With subsequent loading cycles, a plastic zone becomes well

established, with the result that the crack tip is shielded from the applied loads. In addition, a cohesive zone develops which has the effect of further limiting the level of stress near the tip. After an initial transient, as quasi-steady mode of growth sets in. It should be carefully noted that, as the amplitude of the loads is held constant, the nominal stress-intensity factor range $\triangle K$ gradually creeps up as a result of the steady increase in crack length.

Fig. 2.6 depicts the contours of effective plastic strain after the crack has grown to a length a =15.7mm under the action of load cycles of amplitude 85MPa. As may be seen, a well-defined plastic wake has formed behind the crack tip. The width of the wake remains ostensibly constant during crack growth. It bears emphasis that the crack grows steadily without evidence of shakedown. As noted earlier, the hysteretic nature of the cohesive law is critical for ensuring steady growth and eliminating spurious crack arrest after a small number of cycles. It is also noteworthy how the mesh resolves the wake for a considerable length behind the tip. Eventually the mesh is coarsened in order to maintain the problem size within reasonable bounds, and some information is inevitably lost. Fig. 2.7 shows a log-log plot of the crack growth rates da/dN predicted by the theory over a broad range of stress-intensity factor amplitudes $\triangle K$. The three computed lines in the figure correspond to the three initial crack lengths: a_0 = 10, 20 and 30 mm. A power-law dependence of da/dN on $\triangle K$ is clearly evident in this plot, which is evidence of Paris-like behavior. Fig. 2.7 shows also a compendium of experimental fatigue data for Aluminum alloys [2]. As may be seen, the experimental data points fall within parallel upper and lower bounds of slope approximately equal to 3. Fig. 2.7a reproduces the experimental bounds and shows that the theoretical lines fall well between them and have ostensibly the same slope.

This comparison demonstrates that the theory is capable of matching long-crack constant-amplitude fatigue data at least as well as Paris's law. It should be carefully noted, however, that the theory is more general than Paris's law, as it does not *a priori* restrict the size or geometry of the crack and the plastic zone, or the time-variation, amplitude or geometry of the loads. The ability of the theory to match the

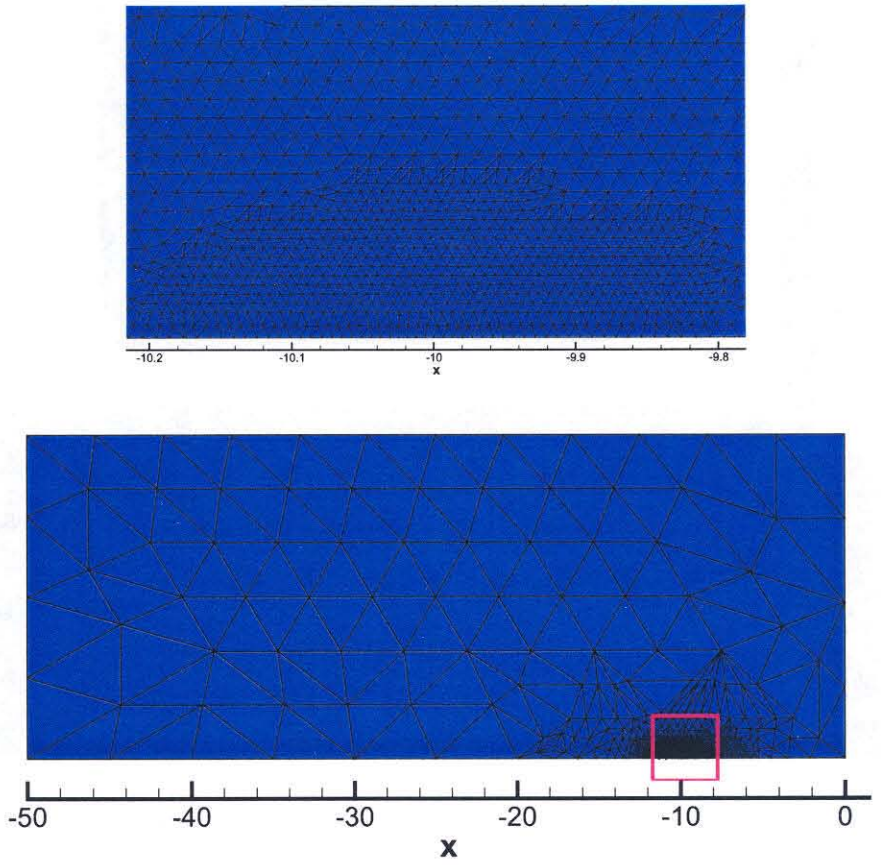

Figure 2.5: Initial mesh, overall view and near-tip detail (crack length $a_0 = 10$ mm).

experimental record outside the range of validity of Paris's law is assessed next.

2.3.2 Short Cracks

It is well-documented experimentally [47, 89] that short cracks exhibit a higher rate of growth than predicted by Paris's law when the material constants in such law are fitted to long-crack data. Thus, for sufficiently short cracks the experimental da/dN–$\triangle K$ data points fail to collapse into a single master curve independent of crack size, and Paris's framework breaks down.

We have assessed the ability of the theory to capture this short-crack effect by considering aluminum center-crack panel specimens with initial crack lengths: $a_0 =$ 1, 5, 10, 20 and 30 mm. The material properties and loading conditions are as in the

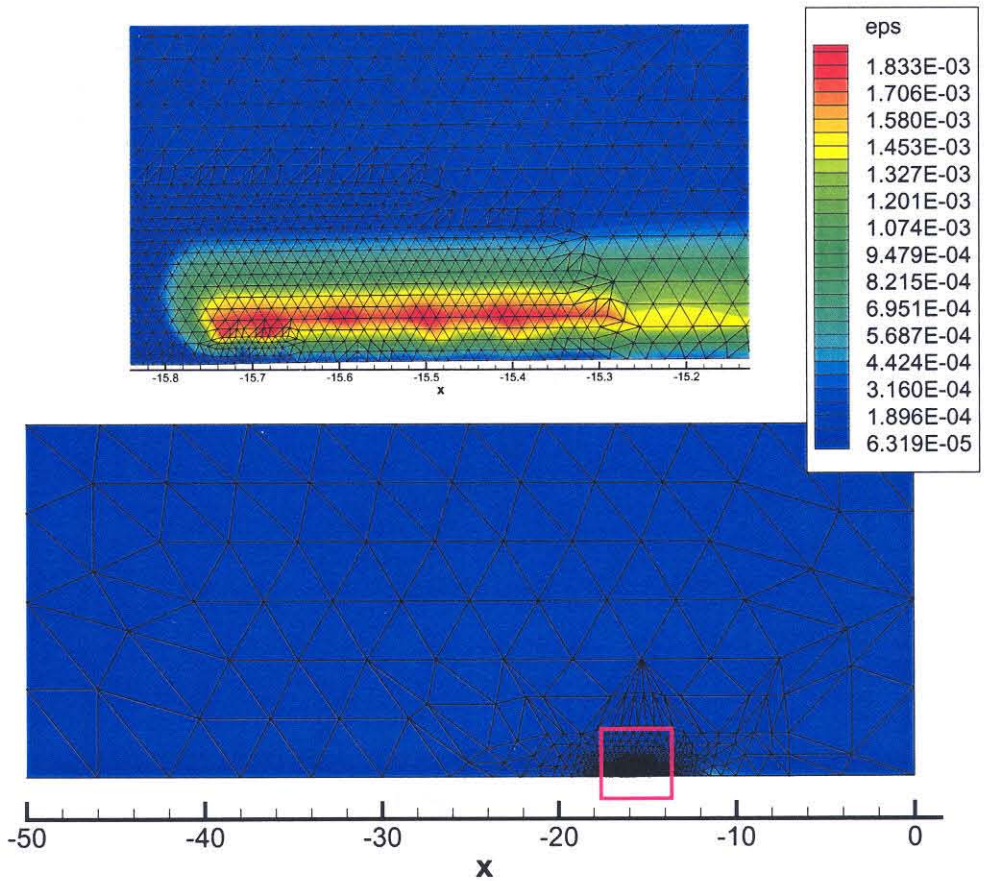

Figure 2.6: Contour plots of effective plastic strain ϵ^p, overall view and near-tip detail (crack length $a = 15.72$ mm).

preceding Section.

Fig. 2.8 collects the predicted crack growth rates. As may be seen from the figure, the rates of growth corresponding to the two longest cracks, $a_0 = 20$ and 30 mm, are almost identical. The slight difference between the two cracks owes mostly to the effect of the boundary of the specimen and the smaller size of the ligament for the 30 mm crack. The near coincidence of the da/dN *vs.* $\triangle K$ curves attests again to the Paris-like behavior predicted by the theory for long cracks. Remarkably, the rates of growth predicted by the (same) theory for the short cracks are greatly in excess of those computed for the long cracks, Fig. 2.8, in keeping with experiment. The theory thus seems to capture the short crack effect. The short crack effect sets in when the

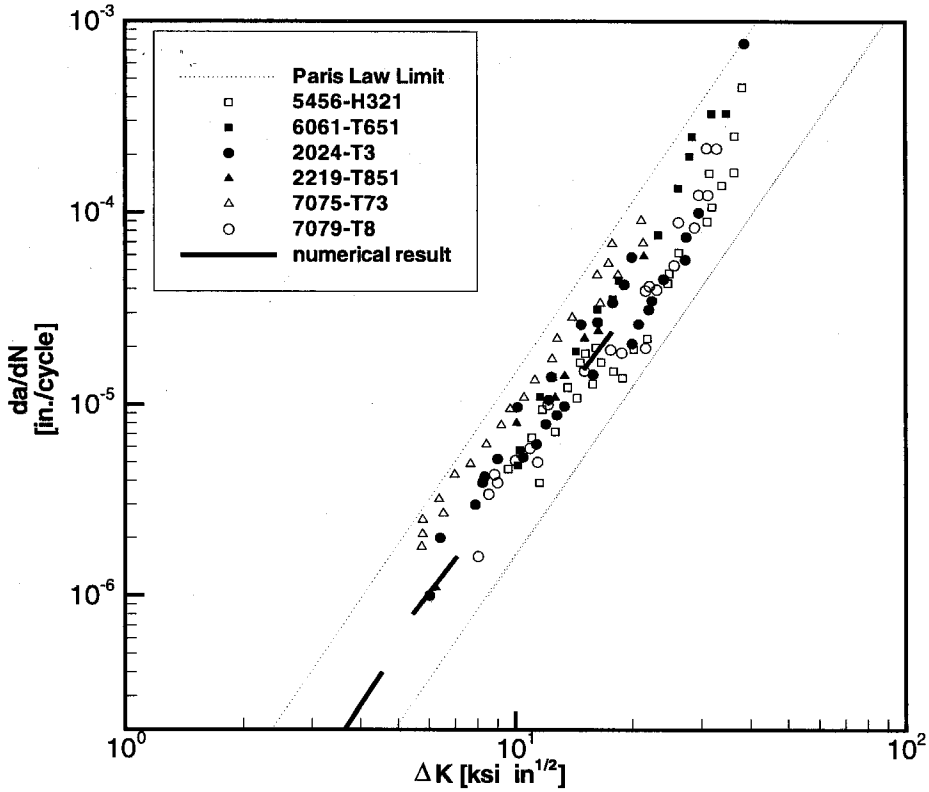

Figure 2.7: Comparison of theoretical and experimental [2] growth rates.

crack size becomes comparable to the size of the cohesive zone, which scales with the characteristic length $l_c = EG_c/T_c^2$. For the material under consideration here this length is $l_c \approx 1.5$ mm, which explains the clear short-crack effect observed in the calculations. Clearly, in this regime the stress intensity factor K no longer provides a measure of the amplitude of the near-tip fields, and it loses its value as a means of interpreting the data and formulating crack-growth laws.

An alternative crack-tip parameter which does retain its meaning irrespective of crack size is the crack-tip opening displacement (CTOD). Based on this observation, Leis *et al.* [47] (see also [41]) suggested a CTOD-based crack-growth law of the form

$$\frac{da}{dN} = C(\Delta\delta)^n \tag{2.21}$$

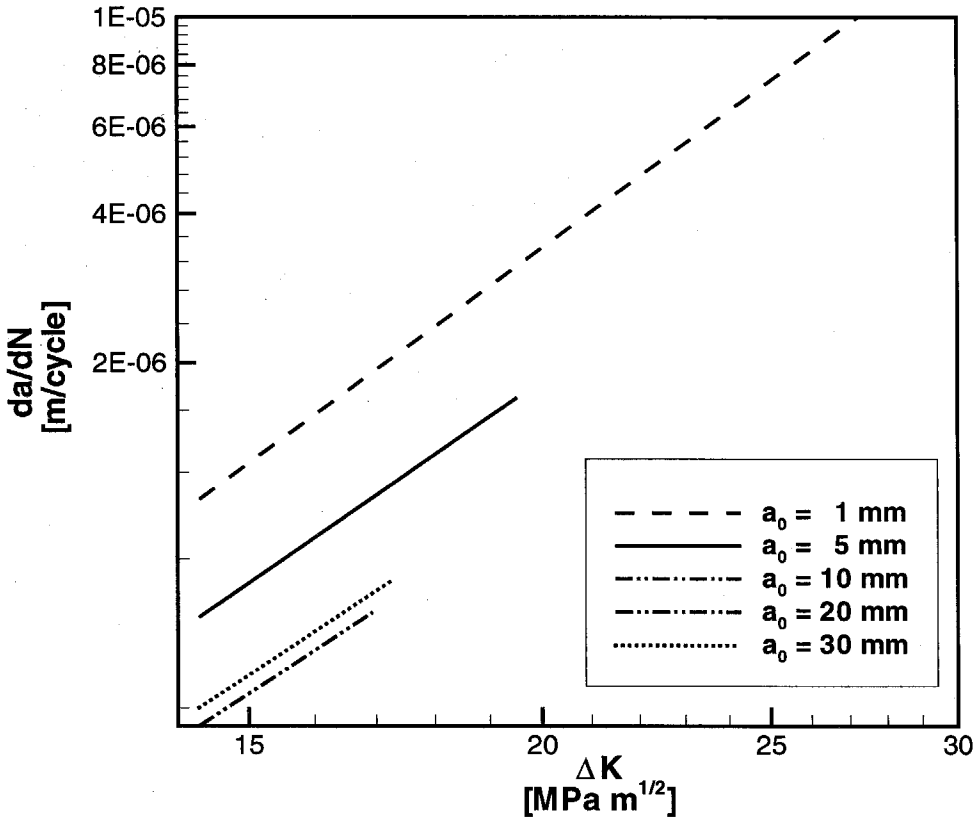

Figure 2.8: da/dN vs. ΔK for different initial cracks sizes: $a_0 = 1,\ 5,\ 10,\ 20,\ 30$mm.

as a means of extending the validity of Paris's law to short cracks. In this expression δ is the CTOD and $\Delta\delta$ is the CTOD range per cycle. Figure 2.9 shows the loci of da/dN–$\Delta\delta$ points predicted by the theory for all crack sizes under consideration. It is evident from the figure that, when plotted against the parameter $\Delta\delta$, all crack growth rates tend to converge on a single master curve. The theory does therefore lend support to Leis *et al.* re-interpretation and extension of Paris's law. The CTOD-based growth law (2.21), if assumed valid, reveals useful insights into the breakdown of Paris's law for short cracks. For simplicity, assume that the applied stress cycles between zero and σ, and that the material is linear elastic. If, in addition, Dugdale's model is assumed to apply, e. g., at the maximum opening displacement δ (cf [10] for

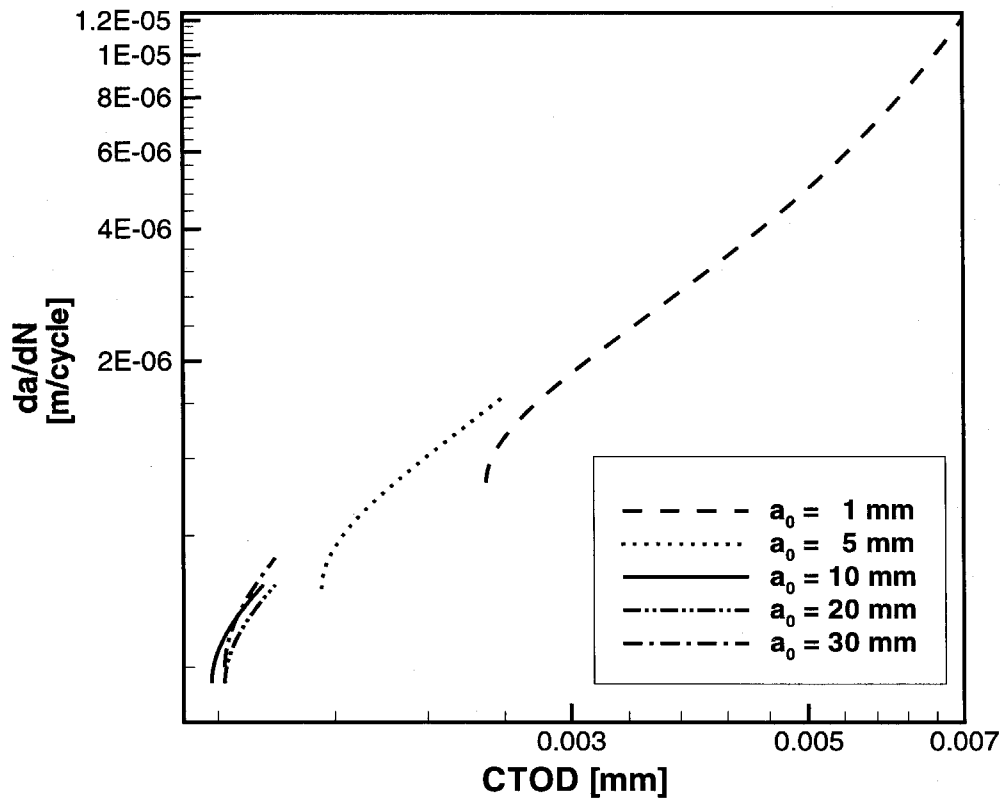

Figure 2.9: Predicted growth rates da/dN *vs.* $\Delta\delta$ for initial crack sizes: a_0 = 1, 5, 10, 20, 30 mm.

a more complete analysis including unloading), then one has, for cracks of any length

$$\delta = \frac{8}{\pi}\frac{T_c}{E} a \log\left[\sec\left(\frac{\pi}{2}\frac{\sigma}{T_c}\right)\right] \tag{2.22}$$

Eliminating σ from (2.22) in favor of the nominal stress-intensity factor $K \equiv \sigma\sqrt{\pi a}$ gives

$$\delta = \frac{8}{\pi}\frac{T_c}{E} a \log\left[\sec\left(\sqrt{\frac{\pi}{a}}\frac{K}{2T_c}\right)\right] \tag{2.23}$$

For long cracks, i. e., when

$$a \gg \frac{\pi}{4}\frac{K^2}{T_c^2} \tag{2.24}$$

Equation (2.23) reduces to

$$\delta \approx \frac{K^2}{ET_c} \tag{2.25}$$

to first order. Thus, in this regime δ is proportional to K^2 and otherwise independent of the crack length, and Paris's law is recovered from (2.21). By way of contrast, when a becomes comparable to $(\pi/4)(K^2/T_c^2)$, the opening displacement δ no longer bears a power relation to K and depends explicitly on the crack size, and Paris's law ceases to apply. Furthermore, if (2.23) is inserted into (2.21), a simple calculation shows that da/dN increases with decreasing a at constant K, in keeping with observation.

2.3.3 The Overload Effect

Paris's law is also known to break down when the crack is subjected to a sudden overload. In particular, it is well documented [93] that one single sharp overload may significantly retard the growth of the crack.

We proceed to assess ability of the theory to capture this overload effect. To this end we consider a center-crack panel of aluminum 2024-T351 of the same dimensions and subject to the same loading conditions as in the calculations discussed in Section 2.3.1. In particular, the initial crack size a_0 is chosen to be 10 mm, the applied stress cycles between zero and 85 MPa, corresponding to $R = 0$ and an initial nominal ΔK of 18 MPa$\sqrt{m}$. In addition to a constant-amplitude calculation such as described in Section 2.3.1, we have carried out a simulation in which, after 500 normal cycles,

the specimen is subjected to one single peak load 50% above nominal. Following the application of the overload, the specimen is again cycled at the original constant amplitude.

Fig. 2.10 shows a comparison of the growth rates predicted with and without overload. As may be seen in Fig. 2.10, the application of the overload causes an instantaneous crack advance followed by crack arrest, or very slow growth, for a period of roughly 200 cycles. Subsequently to this temporary slowdown, the growth rate increases steadily and tends to the growth constant-amplitude rate. However, the application of the overload results in a permanent lag in the size of the crack and, consequently, in an extension of the fatigue life of the specimen. These trends are in excellent agreement with the available observational evidence (e. g., [93]).

The response just described is the result of several competing mechanisms. Thus, the application of the overload raises the driving force for crack-growth and the crack shoots forward instantaneously. However, the overload also causes the plastic zone to grow in size markedly. Upon unloading, the residual stresses associated with this plastic deformation tend to close the crack, with an attendant slowdown in the subsequent growth rate.

2.4 Summary and Conclusions

We have investigated the use of cohesive theories of fracture, in conjunction with the explicit resolution of the near-tip plastic fields and the enforcement of closure as a contact constraint, for the purpose of fatigue-life prediction. The cohesive law formulated as part of the theory has the distinguishing characteristic of exhibiting unloading-reloading hysteresis. The inclusion of unloading-reloading hysteresis into the cohesive law simulates simply dissipative mechanisms such as crystallographic slip and frictional interactions between asperities, and the accumulation of damage within the cohesive zone, eventually leading to complete decohesion and crack extension. Consideration of unloading-reloading hysteresis also has the important consequence of preventing shakedown, thus allowing for steady crack growth.

The calculations explicitly resolve all plastic fields and cohesive lengths and, consequently, the theory is free from the restrictions needed to ensure small-scale yielding. In particular, the theory does not directly rely on the stress-intensity factor as a crack-tip loading parameter. Our calculations demonstrate that the theory is capable of a unified treatment of long cracks under constant-amplitude loading, short cracks and overloads. In the case of long cracks and constant-amplitude loads, the theory predicts Paris-like behavior, i. e., the rate of growth is in proportion to a certain power of the stress-intensity factor range and is independent of the length of the crack. By way of contrast, the *same* theory predicts the experimentally observed growth acceleration in the short-crack regime, as well as the equally observed growth retardation due to overloads, without *ad hoc* corrections or tuning.

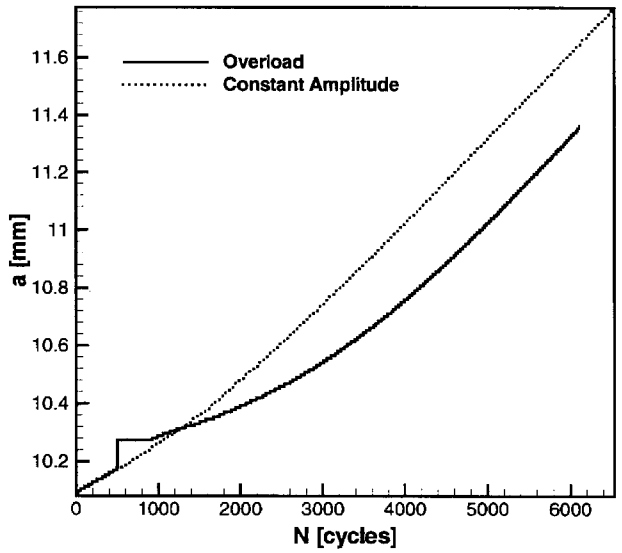

(a)

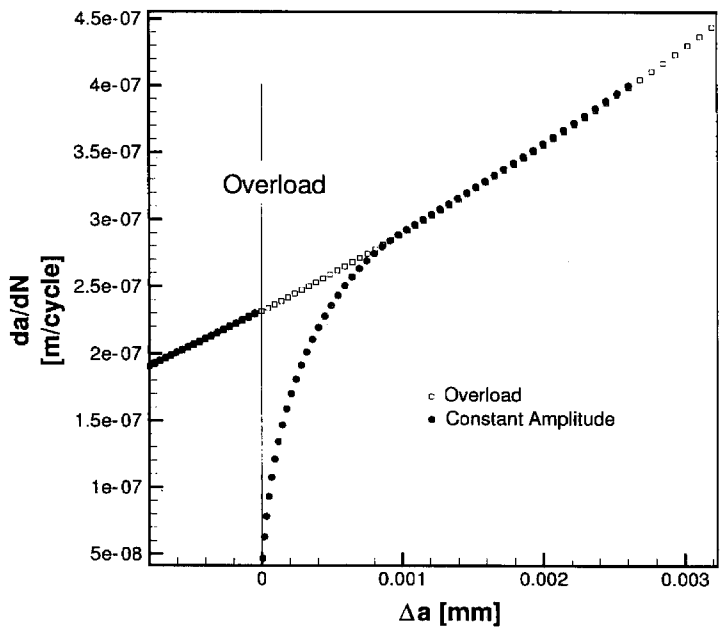

(b)

Figure 2.10: (a) Fatigue life curve and (b) growth rates for a constant-amplitude loading with and without a single 50% overload at the 500th cycle.

Chapter 3 A Cohesive Model of Fatigue Crack Initiation

3.1 Introduction

We extend the fatigue crack growth model presented in Chapter 2 to account for fatigue initiation. The crack lengths involved at initiation may vary from the order of micrometers if studied at the microscopic level to the orders of millimeters at the macroscopic level. We adopt here an engineering perspective, focusing our attention to initiation of cracks at the macroscopic scale. Fatigue initiation may therefore be related to the detection of the smallest crack resolved by current crack detection systems.

The engineering approach to fatigue initiation is characterized in terms of the number of (stress or strain) cycles necessary to induce fatigue failure in a smooth, initially uncracked specimen. Although this is a *total-life* approach, it measures fatigue initiation to a good approximation as the fatigue life propagation in these specimen is small compared to the fatigue initiation. The pioneer of the stress-life approach is Wohler [98], who was the first to define the concept of endurance or fatigue limit. Several phenomenological laws for fatigue initiation were derived from such an approach in order to account for the influence of the applied stress range, mean stress,... on the number of cycles to initiation. Some relations to account for effect of the mean stress have been proposed by Gerber [29], Goodman [33], Basquin [5], Soderberg [86], and Morrow [53]. In order to account for variable amplitude loading, Palmgren [67] and Miner [51] have suggested the Palmgren-Miner cumulative damage rule. The strain-life approach has been led by Coffin [13] and Manson [49] who derived the so-called Coffin-Mansion relationship.

Our objective is to unify some of the empirical models by having recourse to the

cohesive theories of fracture. We restrict our attention to a candidate material point from which a fatigue crack could initiate. Our objective is to determine the number of cycles to failure for that material point as a function of load parameters, e. g., maximum load, minimum load, etc.

The chapter is structured as follows. The essential elements of the fatigue initiation model can be found in Section 3.2. Subsection 3.2.1 describes the cohesive law under monotonic and cyclic loading. Subsection 3.2.2 presents our model of fatigue initiation. Finally, Section 3.3 shows several examples of applications and comparison with experimental data found in the literature.

3.2 Fatigue Initiation Model

We place ourselves within the framework of the cohesive theories of fracture. Crack formation is considered as a gradual separation of material surfaces resisted by cohesive tractions. A number of cohesive models have been suggested to describe monotonic fracture processes [55, 57, 61, 11, 91, 16, 68]. In Chapter 2, we proposed a cohesive model fracture under cyclic loading. The fatigue initiation model we suggest here relies on these two approaches.

3.2.1 Cohesive Law for fatigue Initiation

Under monotonic loading, the separation of the material surfaces is gradual and governed by a cohesive law which may vary in shape. We adopt the universal binding energy-distance relationship (UBER) [81] as our monotonic cohesive law:

$$\sigma(\delta) = C\delta \exp(-\frac{\delta}{\delta_0}) \tag{3.1}$$

where C and δ_0 are material constants, and δ is the opening displacement. As may be recalled, we assume the cohesive response of material surfaces to be rigid prior to the attainment of the cohesive strength of the material. Therefore, we slant the UBER

relation so as to eliminate its initial elastic stiffness:

$$T(\delta) = \sigma(\delta + \frac{T(\delta)}{C}) \tag{3.2}$$

where $T(\delta)$ defines the slanted (or equivalently elastically corrected) cohesive law under monotonic loading; see Fig. 3.1(a). We will subsequently refer to equation 3.2 as the monotonic cohesive envelope.

As the potential fracture surface starts to open under the action of the loads, the opening is resisted by a number of material-dependent mechanisms such as cohesion at the atomistic scale, bridging ligaments, interlocking of grains and others. The maximum applied monotonic load a material point on a cohesive surface could sustain is given by T_c and the corresponding opening displacement is δ_c. Any applied load above T_c will result in the failure of the cohesive material surface. In that case, only one cycle is needed for crack initiation and the opening displacement at initiation is δ_c. If the maximum applied load upon monotonic loading is less than T_c, the material does not fail and crack nucleation does not occur.

A variation of the cohesive envelope defined by equation 3.2 is also considered in this model. We introduce a threshold value of the cohesive stress $T_{threshold}$, as shown in Fig. 3.1(b). $T_{threshold}$ simply prevents the opening of an initially closed material surface if subjected to applied stresses below $T_{threshold}$.

Under cyclic loading, we adopt the irreversible cohesive law with unloading-reloading hysteresis developed in Chapter 2; see Fig. 3.2. We assume that the cohesive traction cannot exceed the monotonic cohesive envelope. Consequently, when the stress-strain curve intersects the envelope during reloading, it is subsequently bound to remain on the envelope for as long as the loading process ensues.

3.2.2 Fatigue Initiation

We consider a candidate material point from which a fatigue crack could initiate. This point can be viewed as belonging to a potential material cohesive surface. The law of separation of such surface is governed by equations 2.2, 2.3 and 2.4 derived

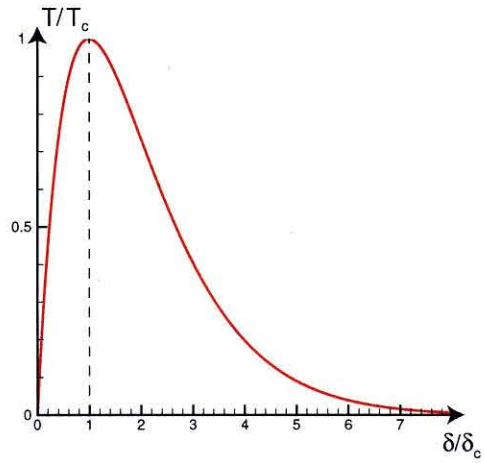

(a) Cohesive Envelope slanted without threshold.

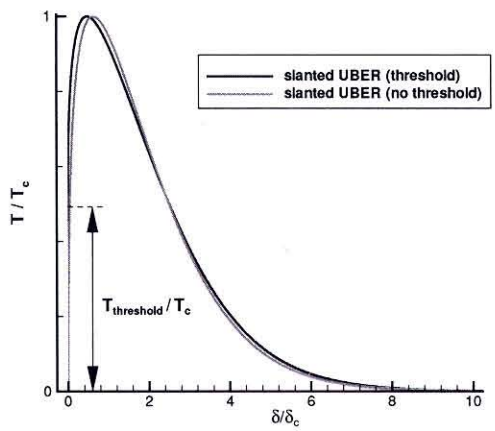

(b) Cohesive Envelope slanted with threshold.

Figure 3.1: Universal binding energy-distance relationship defining the monotonic cohesive envelope for the cohesive law of fatigue initiation.

in Chapter 2. These equations define the model I of fatigue initiation. We have also considered a second model (model II) for which K^+ had slightly different kinetic equations. In model II, we postulate that upon unloading, K^+ becomes equal to K^-, i.e., δ_f is set to zero in equation 2.4 if $\dot{\delta} < 0$.

Let us denote by δ the opening displacement of the material point and by $t(\delta)$ the

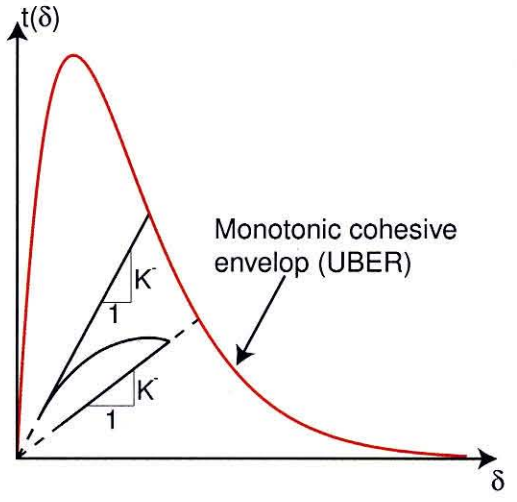

Figure 3.2: Cyclic cohesive law with unloading-loading hysteresis.

corresponding cohesive traction. In order to determine the number of cycles to failure as a function of loading parameters, the material point under consideration is cycled between a maximum and minimum applied stress, denoted respectively by σ_{max} and σ_{min}. A possible path followed by the candidate material point in the space (t,δ) is schematized in Fig. 3.3, where σ_{min} and σ_{max} are assumed to remain constant for the sake of clarity.

Following the first loading to σ_{max}, the material point reaches C_1. Upon unloading to σ_{min}, the first cycle is completed. After a series of four cycles, the material point reaches C_5 and it is clear from Fig. 3.3 that the cohesive traction cannot sustain the applied stress σ_{max}. The material surfaces have reached a state where the opening displacement grows unbounded under the applied loads. This onset defines fatigue crack initiation and is characterized by a critical opening displacement, $\delta_{initiation}$, beyond which the cohesive tractions cannot sustain the maximum load of the fatigue cycle.

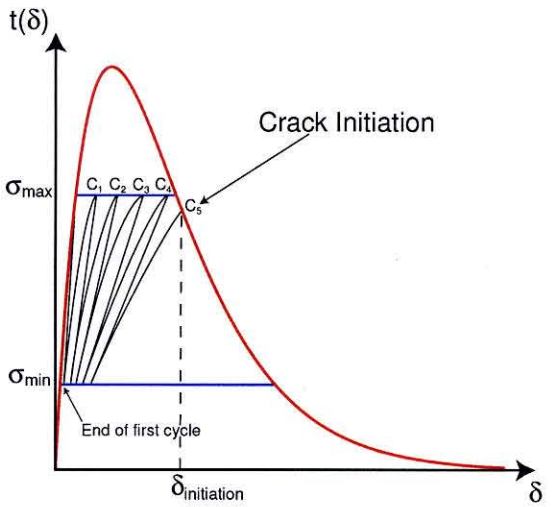

Figure 3.3: Cyclic cohesive law with a UBER-type monotonic envelope. Fatigue nucleation process.

3.3 Applications

3.3.1 The Fatigue Limit

We proceed to compare experimental data of constant-amplitude fatigue tests of smooth specimen of aluminum 2024-T4 alloy [35] (table 3.1) with the model developed previously. The parameters of the cohesive envelope were adjusted so that T_c corresponds to the ultimate tensile strength of the material and the area under the cohesive envelope is equal to the macroscopic fracture energy. Two parameters are available to fit the experimental data: $T_{threshold}$ and the decay parameter δ_f, defined perviously in Chapter 2. For both models I and II, we find that without threshold, the optimal δ_f is equal to 6 mm, whereas with threshold, δ_f is 40 mm and T_c is 127.5 MPa. The numerical results in Fig. 3.4 reveal that the difference between models I and II is significant mainly in the low cycles-to-failure regime. In that regime, the applied stress is close to the ultimate tensile strength and it is expected that a specimen under such high stress should fail almost immediately. The S-N curve obtained from the model II is characterized by a critical value of the applied stress above which the

Al 2024-T4	
Specific cohesive energy G_c	13.6 kJ/m^2
Cohesive strength T_c	503 MPa
Al 2048-T851	
Specific cohesive energy G_c	13.04 kJ/m^2
Cohesive strength T_c	455 MPa
Steel 300M	
Specific cohesive energy G_c	16.38 kJ/m^2
Cohesive strength T_c	1930 MPa

Table 3.1: Material constants used in the fatigue initiation calculations.

specimen fails in one cycle. On the other hand, S-N curves determined from model I do not have that characteristic. Instead, with model I, the S-N curves are very flat for applied loads just below the ultimate tensile strength. One would therefore predict lifes as high as 10^4 cycles for specimens subjected to loads barely under the ultimate tensile strength.

At lower applied stress, both models with threshold fall in the ball park of the experimental data, while the models without threshold tend to overestimate the life of the specimen.

3.3.2 Mean Stress Effect on Fatigue Life

The effect of the mean stress on the fatigue life is shown in Figs. 3.5 and 3.6, where we compare experimental data [36, 37] for steel 300M and Aluminum 2048-T851 alloy (table 3.1). We find that δ_f is 50. mm and T_c is 180 MPa for the Al2048-T851; δ_f is 0.9 mm and T_c is 950 MPa for the Steel 300M. From these figures, we observe that model I appears to fit better the experimental data for the first part of the S-N curve. However, neither of the models seem to do well for the tail of the S-N curve and deviate significantly from the experimental data.

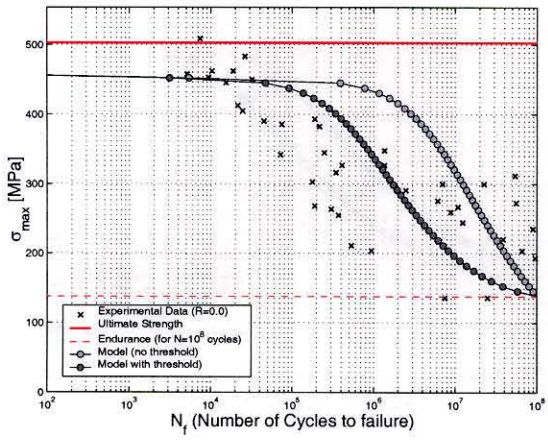

(a) Aluminum 2024-T4, Model 1.

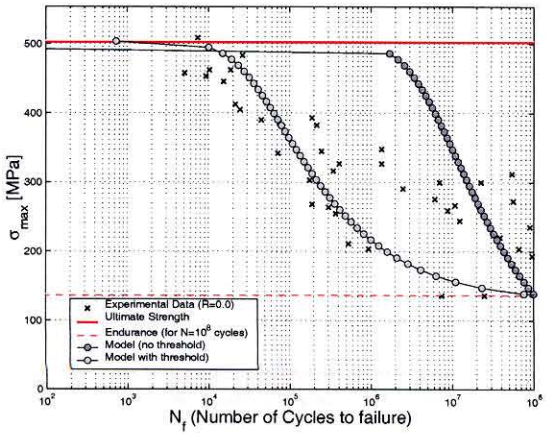

(b) Aluminum 2024-T4. Model 2.

Figure 3.4: Comparison between the two models with and without threshold and the experimental data of Aluminum 2024-T4.

3.4 Conclusions

We have derived a model of fatigue initiation based on a hysteretic cohesive law with a UBER type envelope corrected to have an infinite slope at the origin. The S-N curves obtained from the model shows reasonable agreement with the experimental data for different types of metals. The model captures the effect of the mean-stress, at least qualitatively. Its simplicity makes it an ideal candidate for a larger scale framework

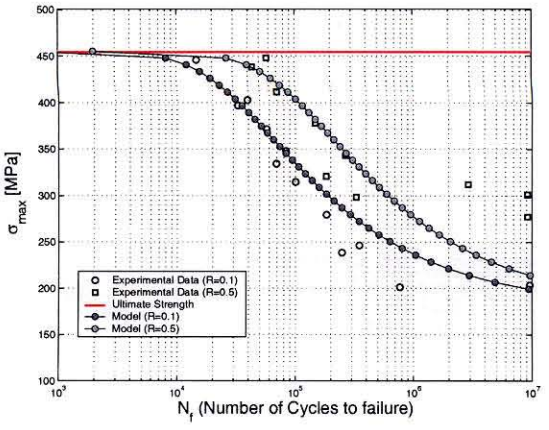

(a) Aluminum 2048-T851. Model 1.

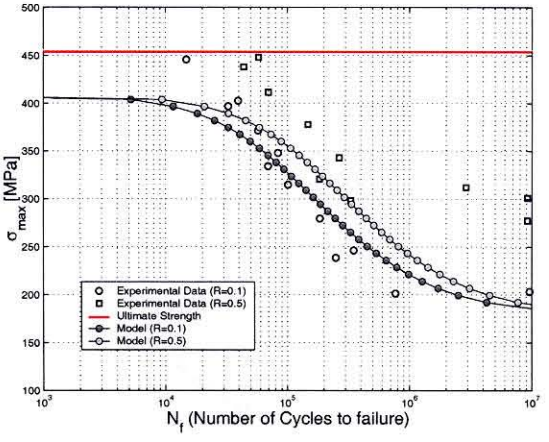

(b) Aluminum 2048-T851. Model 2.

Figure 3.5: Comparison between Model I and II when $R = \sigma_{min}/\sigma_{max}$ is non-zero.

in order to study more complex problems such as the environmental, temperature, plasticity and multi-axial loading effect on fatigue nucleation.

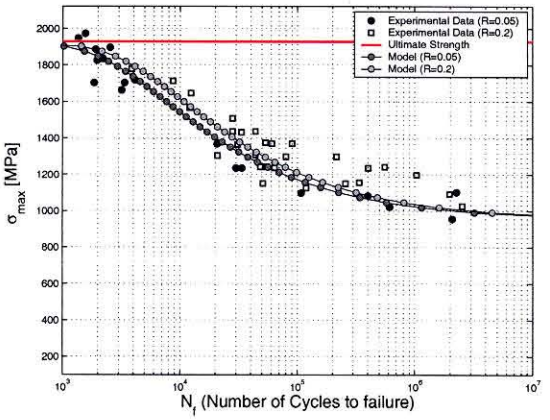

(a) Steel 300M. Model 1.

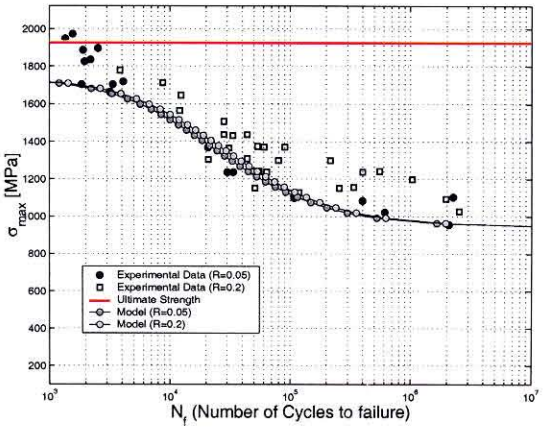

(b) Steel 300M. Model 2.

Figure 3.6: Comparison between Model I and II when $R(\sigma_{min}/\sigma_{max})$ is non-zero.

Chapter 4 Coarse-Graining and Renormalization of Atomistic Binding Relations and Universal Macroscopic Cohesive Behavior

4.1 Introduction

Cohesive theories of fracture are predicated on a direct description of the physical processes which lead to separation and the eventual formation of a free surface. The development of cohesive theories rests on a detailed physical understanding of the operative fracture mechanisms, which are often complex and cut across multiple lengthscales, especially where ductile fracture is concerned. Cleavage fracture, by way of contrast, entails the simple separation of atomic planes and is, therefore, governed by interplanar potentials which are amenable to an effective first-principles atomistic characterization. For instance, Jarvis *et al.* [39] have recently calculated the cohesive behavior of (111) planes in fcc aluminum, and of Al_2O_3 cleavage planes, using GGA density functional theory; and Park and Kaxiras [72] have carried out ab-initio simulations of hydrogen embrittlement in aluminum and calculated generalized stacking-fault energies as a function of interplanar separation and sliding.

First-principles interplanar potentials are characterized by peak stresses of the order of the theoretical strength of the crystal. In addition, the crystal loses its bearing capacity after an interplanar separation of only a few angstroms. Moreover, the integration of first-principles interplanar potentials into engineering calculations necessitates full atomistic resolution in the vicinity of the crack tip, which is often unfeasible or impractical. This disconnect between atomistic and engineering descriptions begs a number of fundamental questions, to wit: What is the proper way

to *coarse-grain* a cohesive description?, and: What is the macroscopic form of the cohesive law after coarse-graining?

In this chapter, we address these issues by investigating the cooperative behavior of a large number of interatomic planes forming a *cohesive layer*. We employ two main approaches in this investigation: relaxation and the renormalization group. Relaxation or *weak convergence* methods are concerned with the determination of the macroscopic behavior of materials characterized by a non-convex energy function. These materials often develop fine microstructure in response to imposed deformations. Truskinovsky *et al.* [17, 75, 18], and Braides *et al.* [8], have pioneered the application of these methods to fracture. However, the full relaxation of a cohesive potential yields the trivial result that the effective cohesive potential is identically equal to zero. The chief difference between the analysis pursued here and full relaxation is that, at zero temperature, we seek energy minimizers of large—*but finite*—collections of interatomic planes. In this limit we find that, for a broad class of interplanar potentials, the macroscopic cohesive law adopts a *universal form* asymptotically.

We show that this universality of the macroscopic cohesive behavior is amenable to a renormalization-group interpretation. The normalization group which coarse-grains the cohesive behavior is somewhat nonstandard and has to be crafted carefully, e. g., so as to preserve the surface energy and the elasticity of the lattice. The universal form of the macroscopic cohesive law is precisely an attractive *fixed point* of the renormalization-group transformation.

4.2 Problem Formulation

We consider a macroscopic cohesive crack opening symmetrically (mode I) and undergoing quasi-static growth. We denote by d the interplanar distance, δ the opening displacement across an interatomic plane, and t the corresponding cohesive traction. These latter variables are presumed related by a known cohesive or binding law $t(\delta)$,

which derives from an interplanar potential $\phi(\delta)$ through the relation

$$t(\delta) = \phi'(\delta) \tag{4.1}$$

Here and subsequently, a prime denotes differentiation of a function of a single variable. For simplicity, we shall assume throughout that the atomistic binding law $t(\delta)$ rises monotonically from zero at $\delta = 0$ to a peak value σ_c at $\delta = \delta_c$, and subsequently decreases monotonically to zero, Fig. 4.1. Correspondingly, the cohesive potential $\phi(\delta)$ is convex in the interval $0 \leq \delta < \delta_c$, has an inflection point at $\delta = \delta_c$, is concave for $\delta > \delta_c$ and asymptotes to twice the surface energy, 2γ, as $\delta \to \infty$. In addition, we shall assume that $\phi(\delta)$ is smooth and analytic at $\delta = 0$, with Taylor expansion:

$$\phi \sim \frac{C}{2}\delta^2 + o(\delta^2) \tag{4.2}$$

for some constant C. The value of C can be readily deduced from the elastic moduli

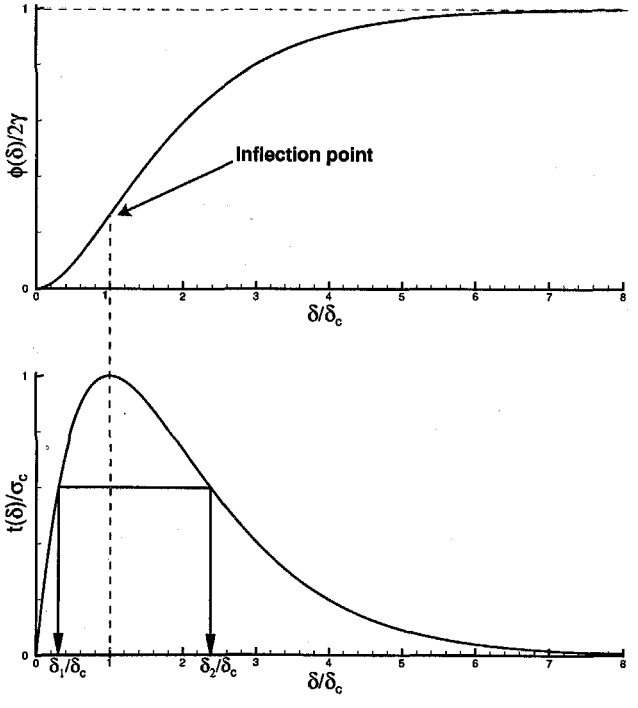

Figure 4.1: Interplanar potential and corresponding cohesive or binding law.

c_{ijkl} of the crystal.[8] To this end, let $\mathbf{m}$ be the unit normal to the plane of the crack, and apply a small and uniform opening displacement to all interatomic planes. Evidently, the energy per unit volume of the crystal follows from the cohesive potential as $(C/2d)\delta^2$ asymptotically as $\delta \to 0$. On the other hand, the strain tensor of the crystal is $\epsilon_{ij} = (\delta/d)m_i m_j$, and the corresponding energy is $(\delta^2/2d^2)c_{ijkl}m_i m_j m_k m_l$. Equating both energies yields the identity:

$$C = \frac{1}{d}c_{ijkl}m_i m_j m_k m_l \tag{4.3}$$

Next imagine that the atomistic description is coarse-grained, e. g., by the quasicontinuum method [90], or by a passage to the continuum limit, or by some other suitable means. Let $\bar{d}$ denote the spatial resolution of the coarse-grained description. For instance, in quasicontinuum or in engineering finite-element simulations $\bar{d}$ measures the local element size. The corresponding effective cohesive law may be obtained by analyzing the behavior of a *cohesive layer* of thickness $\bar{d}$ and containing $N = \bar{d}/d$ atomic planes. The cohesive layer is taken through a total opening displacement $\bar{\delta}$ resulting in a macroscopic traction $\bar{t}$. The chief objective of the analyses that follow is to determine the macroscopic cohesive law $\bar{t}(\bar{\delta})$ in the limit of N large but finite. Equivalently, we may seek to determine the asymptotic form of the macroscopic cohesive potential $\bar{\phi}(\bar{\delta})$ such that

$$\bar{t}(\bar{\delta}) = \bar{\phi}'(\bar{\delta}) \tag{4.4}$$

in the same limit.

4.3 Universal Asymptotic Form of the Macroscopic Cohesive Law at Zero Temperature

At zero temperature, the crystal deforms so as to minimize its total energy. The governing principle is, therefore, energy minimization. Let $\delta_i \geq 0$, $i = 1, \ldots, N$ be

the opening displacements of the interatomic planes in the cohesive layer. Then, the total energy of the cohesive layer is

$$E^{\text{tot}} = \sum_{i=1}^{N} \phi(\delta_i) \tag{4.5}$$

Let now $\bar{\delta}$ be the macroscopic opening displacement. Then, the effective or macroscopic energy of the cohesive layer follows from the constrained minimization problem:

$$\bar{\phi}(\bar{\delta}) = \inf_{\{\delta_1,\ldots,\delta_N\}} \sum_{i=1}^{N} \phi(\delta_i) \tag{4.6}$$

$$\bar{\delta} = \sum_{i=1}^{N} \delta_i \tag{4.7}$$

In conjunction with the kinematic constraints (4.7), the stationarity of E^{tot} demands

$$t(\delta_i) = \bar{t}(\bar{\delta}) = \text{constant}, \quad i = 1, \ldots, N \tag{4.8}$$

Thus, at equilibrium, all interplanar tractions must be equal to the macroscopic traction.

We shall classify the possible states of an interatomic plane into two categories or *variants*, according as to whether the opening displacement δ is in the range $0 \leq \delta < \delta_c$, or in the range $\delta > \delta_c$. We shall designate variants of the first kind as *coherent*, and variants of the second kind as *decohered*. We may further classify the states of a cohesive layer by the number N_1 of coherent planes, or, equivalently, the number N_2 of decohered planes, it contains. Since the function $t(\delta)$ is one-to-one over the interval $[0, \delta_c)$, equation (4.8) demands that the opening displacements of all coherent planes be equal at equilibrium. Likewise, the opening displacements of all decohered planes must be identical at equilibrium. Under these conditions the macroscopic cohesive

energy follows from the minimization problem:

$$\bar{\phi}(\bar{\delta}) = \inf_{\{(\delta_1,\delta_2),(N_1,N_2)\}} \{N_1\phi(\delta_1) + N_2\phi(\delta_2)\} \tag{4.9}$$

$$\bar{\delta} = N_1\delta_1 + N_2\delta_2 \tag{4.10}$$

$$N = N_1 + N_2 \tag{4.11}$$

$$0 \leq \delta_1 < \delta_c \tag{4.12}$$

$$\delta_2 > \delta_c \tag{4.13}$$

where δ_1 and δ_2 are the opening displacements in the coherent and decohered planes, respectively. In addition, the equilibrium equations (4.8) reduce to

$$t(\delta_1) = t(\delta_2) = \bar{t}(\bar{\delta}) \tag{4.14}$$

These relations are depicted geometrically in Fig. 4.1.

Next we proceed to determine the minimum energy states of a cohesive layer by analyzing the cases $N_2 = 0, 1, 2, \ldots$ in turn. We begin by considering the case in which all planes are coherent, corresponding to $N_1 = N$ and $N_2 = 0$. Then, the kinematic constraint (4.7) gives $\delta_1 = \bar{\delta}/N \equiv \delta$. Evidently, in the limit of $N \to \infty$, δ tends to zero and, in view of equations. (4.2) and (4.9), we obtain

$$\bar{\phi}(\bar{\delta})\big|_{N_2=0} \sim \frac{\bar{C}}{2}\bar{\delta}^2, \qquad \text{as } N \to \infty \tag{4.15}$$

where

$$\bar{C} = \frac{C}{N} \tag{4.16}$$

is an effective cohesive-layer stiffness.

Consider next the case of one decohered plane, $N_1 = N - 1$ and $N_2 = 1$, whence (4.10) becomes

$$(N-1)\delta_1 + \delta_2 = \bar{\delta} \tag{4.17}$$

Solving for δ_1 gives $\delta_1 = (\bar{\delta} - \delta_2)/(N-1)$. In addition, since δ_i and $\bar{\delta}$ are required to

be nonnegative, it follows that $\delta_1 \leq \bar{\delta}/(N-1)$, and thus $\delta_1 \to 0$ as $N \to \infty$. From this limit it additionally follows that $\delta_2 \to \bar{\delta}$ in the same limit. Suppose now that $\bar{\delta} \gg \delta_c$ and, hence, $\delta_2 \gg \delta_c$. Under these conditions, $\phi(\delta_2) \sim 2\gamma$ and (4.9) reduces to

$$\bar{\phi}(\bar{\delta})\big|_{N_2=1} \sim 2\gamma, \qquad \text{as } N \to \infty \tag{4.18}$$

Since interactions beyond nearest neighbors are not taken into account, an altogether identical analysis gives

$$\bar{\phi}(\bar{\delta})\big|_{N_2=k} \sim 2k\gamma, \qquad \text{as } N \to \infty \tag{4.19}$$

for the case of k decohered planes.

The macroscopic cohesive energy may now be expressed as

$$\bar{\phi}(\bar{\delta}) = \min_{0 \leq k \leq N} \bar{\phi}(\bar{\delta})\big|_{N_2=k} \tag{4.20}$$

However, it follows from (4.19) that, asymptotically as $N \to \infty$, multiple decohered planes are not energetically possible at zero temperature, and only the cases $k = 0$ and $k = 1$ need be considered in (4.20). Therefore, the effective cohesive potential is the lower envelope of the energies (4.15) and (4.18), namely,

$$\bar{\phi}(\bar{\delta}) = \min\{\frac{\bar{C}}{2}\bar{\delta}^2, 2\gamma\} = \begin{cases} (\bar{C}/2)\bar{\delta}^2, & \text{if } \bar{\delta} < \bar{\delta}_c \\ 2\gamma, & \text{otherwise} \end{cases} \tag{4.21}$$

where

$$\bar{\delta}_c = 2\sqrt{\frac{\gamma}{\bar{C}}} = 2\sqrt{\frac{\gamma N}{C}} \tag{4.22}$$

is a macroscopic critical opening displacement for the nucleation of a single decohered plane. The corresponding macroscopic cohesive law is

$$\bar{t}(\bar{\delta}) = \begin{cases} \bar{C}\bar{\delta}, & \text{if } \bar{\delta} < \bar{\delta}_c \\ 0, & \text{otherwise} \end{cases} \tag{4.23}$$

It is interesting to note that the peak macroscopic traction is

$$\bar{\sigma}_c = \bar{C}\bar{\delta}_c = 2\sqrt{\bar{C}\gamma} = 2\sqrt{\frac{C\gamma}{N}} \tag{4.24}$$

We conclude the analysis by verifying that, in the decohered regime, $\bar{\delta} > \bar{\delta}_c \sim \sqrt{N}$, and hence $\bar{\delta} \gg \delta_c$ for sufficiently large N, as supposed.

These functions are shown in Fig. 4.2. The macroscopic cohesive potential is initially quadratic and subsequently constant following the attainment of the critical macroscopic opening displacement. Remarkably, the macroscopic critical opening displacement and peak traction scale as: $\bar{\delta}_c \sim \sqrt{N}$ and $\bar{\sigma}_c \sim 1/\sqrt{N}$, respectively. Thus, for large N, it follows that the macroscopic cohesive law entails much lower tractions, occurring at much larger opening displacements, than the atomistic binding law. In effect, the passage from the atomistic to the macroscopic scales is accompanied by an expansion of the opening displacement axis and a simultaneous compression of the traction axis. By constrast, the macroscopic fracture energy, or critical energy-release rate, $\bar{\phi}(\infty)$ remains invariant under the transformation and is equal to the atomistic value $\phi(\infty) = 2\gamma$. It is also remarkable that, for the class of binding laws under consideration, the asymptotic form (4.21) of the macroscopic cohesive law is *universal*, i. e., independent of the atomistic binding law. Evidently, the parameters which define the macroscopic cohesive law quantitatively, e. g., the surface energy γ and the modulus C, are material specific.

As a simple illustrative example, we consider the universal binding energy relation (UBER) [81] defined by the interplanar potential:

$$\phi(\delta) = 2\gamma - C\delta_c(\delta + \delta_c)e^{-\delta/\delta_c} \tag{4.25}$$

This function falls within the class of potentials considered in the foregoing. We choose as material constants: $C = 3.54$ J/m^2/Å^2, $\delta_c = 0.66$ Å, which are representative of aluminum. The macroscopic cohesive laws resulting from a direct numerical minimization of the energy (4.9) for different values of N are shown in Fig. 4.3. The

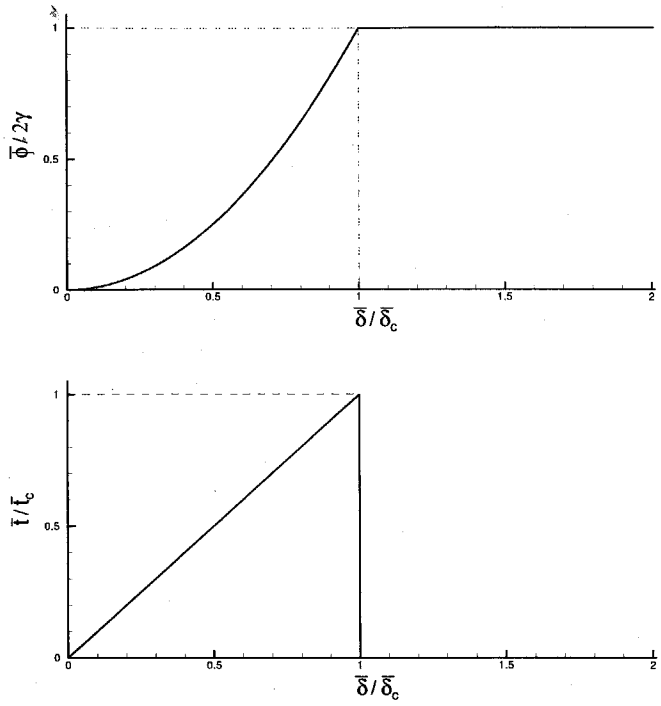

Figure 4.2: Universal asymptotic form of the macroscopic cohesive law at zero temperature.

universal asymptotic form of the macroscopic cohesive law is compared in Fig. 4.4 against the corresponding numerical results. The convergence of the macroscopic cohesive law towards the universal asymptotic form as the number of planes in the cohesive layer increases is clearly evident in this figure.

4.4 Effect of Finite Temperature

At finite temperature, entropic effects make it feasible for the cohesive layer to decohere on multiple planes. In order to assess this effect simply, we recall that, asymptotically, the energy of a cohesive layer with no decohered planes is $(\bar{C}/2)\bar{\delta}^2$, and that the energy of a cohesive layer containing k decohered planes is $2k\gamma$. Within this

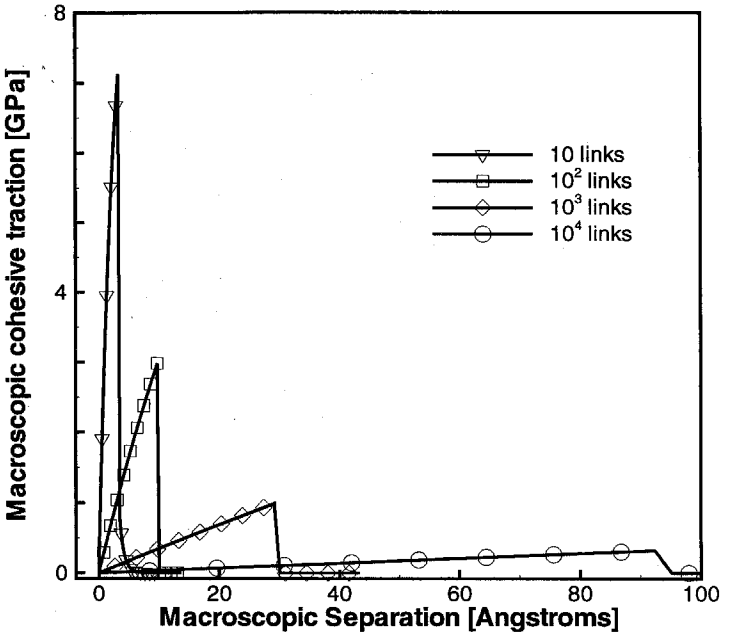

Figure 4.3: Numerically computed macroscopic traction *vs.* opening displacement relation for an increasing number of atomic planes in the cohesive layer.

approximation, the partition function of an area a^2 of layer is, therefore,

$$Z(\bar{\delta},T) = \mathrm{e}^{-\beta(\bar{C}/2)\bar{\delta}^2 a^2} + \sum_{k=1}^{\infty} \mathrm{e}^{-\beta 2k\gamma a^2} \tag{4.26}$$

where $\beta = 1/k_B T$, and k_B is Boltzmann's constant. In order to count states properly, we identify a with the lattice parameter of the crystal. Physically, this is tantamount to allowing for decohered areas of a size commensurate with the lattice parameter. The sum in (4.26) defines a geometric series which may be evaluated readily, with the result:

$$Z(\bar{\delta},T) = \mathrm{e}^{-\beta(\bar{C}/2)\bar{\delta}^2 a^2} + \frac{\mathrm{e}^{-\beta 2\gamma a^2}}{1-\mathrm{e}^{-\beta 2\gamma a^2}} \tag{4.27}$$

The free energy density per unit area of the layer now follows as

$$\bar{F}(\bar{\delta},T) = -\frac{1}{a^2}\frac{1}{\beta}\log Z(\bar{\delta},T) \tag{4.28}$$

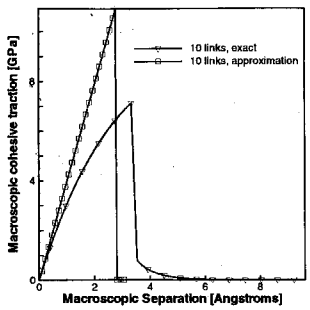

(a) $N = 10$.

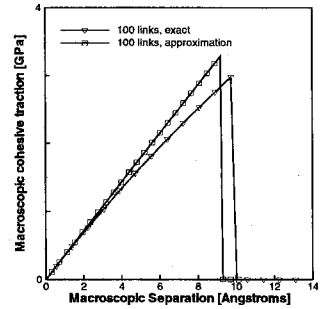

(b) $N = 100$.

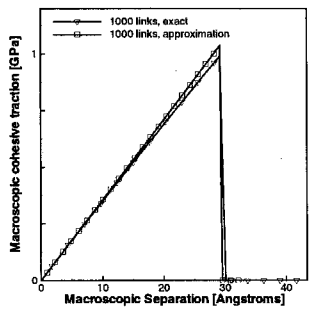

(c) $N = 1000$.

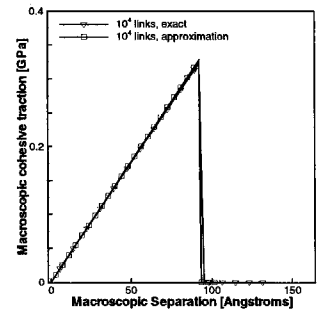

(d) $N = 10^4$.

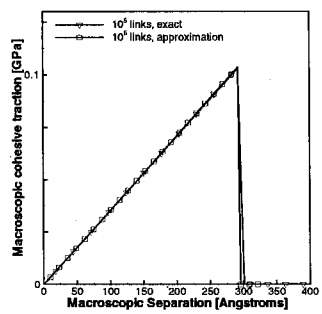

(e) $N = 10^5$.

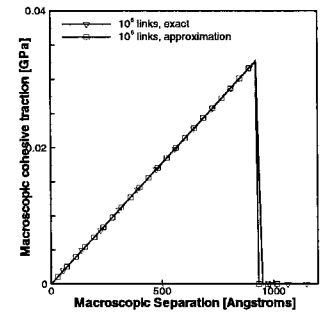

(f) $N = 10^6$.

Figure 4.4: Comparison between numerically computed macroscopic cohesive law and universal asymptotic form for an increasing number of atomic planes in the cohesive layer.

whereas the resulting effective cohesive law is

$$\bar{t}(\bar{\delta},T) = \frac{d\bar{F}}{d\bar{\delta}}(\bar{\delta},T) \tag{4.29}$$

The effect of temperature on the macroscopic cohesive potential for aluminum, endowed with an interplanar potential of the UBER type, is shown in Fig. 4.5. The lattice parameter is taken to be $a = 4.05$ Å. As expected, the Helmholtz free energy rises above the zero-temperature in the amount TS, where S is the configurational entropy of the layer, Fig. 4.5a. The corresponding effect on the macroscopic cohesive law is to smooth out the decohesion transition, Fig. 4.5b.

4.5 Renormalization Group Interpretation

The renormalization group (RG) (see, e. g., [32]) provides a natural framework for the understanding of universality, i. e., the phenomenon that large classes of systems with unrelated Hamiltonians may nevertheless exhibit identical thermodynamic behavior near critical points. It is therefore not entirely unexpected that the main result of Section 4.3, namely, that the limiting form of the potential of a cohesive layer is universal for a broad class of interplanar potentials, can be given a compelling interpretation within the RG framework.

For simplicity, we confine our attention to the zero temperature case. We proceed to construct an RG transformation R such that the sequence

$$\phi_{n+1} = R\phi_n, \quad n = 0, 1, \ldots \tag{4.30}$$

with $\phi_0(\delta) = \phi(\delta)$, yields, by recourse to an appropriate scaling, the large N asymptotic form of the macroscopic cohesive law in the limit. As in the preceding Section, the interplanar potentials contemplated here, and to which the transformation R is applied, are continuous, monotonically increasing functions $\phi : [0, \infty) \to [0, 2\gamma]$ and analytic at the origin. For simplicity, we additionally restrict attention to functions $\phi(\delta)$ possessing a single inflection point, so that $\phi'(\delta)$ has a single maximum.

We construct R by the usual combination of decimation and scaling. The decimation step concerns a layer consisting of two interatomic planes with opening displacements δ_1 and δ_2 and total opening displacement δ. The corresponding effective energy follows from the minimization problem:

$$\tilde{\phi}(\delta) = \inf_{\{\delta_1,\delta_2\}} \{\phi(\delta_1) + \phi(\delta_2)\} \tag{4.31}$$

$$\delta = \delta_1 + \delta_2 \tag{4.32}$$

Next, we proceed to rescale $\tilde{\phi}(\delta)$ in such a way that the sequence defined by (4.30) has a well-defined fixed point. Since the transformation must preserve the relation $\phi(\infty) = 2\gamma$, it is clear that we are allowed to rescale the independent variable δ only. Thus, we set

$$(R\phi)(\delta) = \tilde{\phi}(\lambda\delta) \tag{4.33}$$

For very small δ the interplanar potential ϕ is essentially quadratic and reflects the elasticity of the lattice. Thus, in order for the transformation to preserve the elasticity of the lattice, it must leave parabolic functions invariant. For $\phi = (C/2)\delta^2$, it follows that $\delta_1 = \delta_2 = \delta/2$ and $\tilde{\phi} = 2(C/2)(\delta/2)^2 = (C/2)(\delta/\sqrt{2})^2$. Finally, $(R\phi)(\delta) = (C/2)(\lambda\delta/\sqrt{2})^2$, whence it follows that $\lambda = \sqrt{2}$ for ϕ to remain invariant under the transformation. The complete RG transformation is, therefore,

$$\tilde{\phi}(\delta) = \inf_{\{\delta_1,\delta_2\}} \{\phi(\delta_1) + \phi(\delta_2)\} \tag{4.34}$$

$$\delta = \delta_1 + \delta_2 \tag{4.35}$$

$$(R\phi)(\delta) = \tilde{\phi}(\sqrt{2}\delta) \tag{4.36}$$

Taking $\delta_1 = 0$ and $\delta_2 = \delta$ in (4.34) immediately shows that the unscaled energy $\tilde{\phi}(\delta)$ is bounded above by the original function $\phi(\delta)$.

It is clear from definition (4.34-4.36) that the RG transformation leaves the specific fracture energy $\phi(\infty)$ invariant and equal to its initial value 2γ. Another invariant of the RG transformation is the initial modulus $C = \phi''(0)$. Indeed, consider the limit of $R\phi$ as $\delta \to 0$. Since necessarily $\delta_1 < \delta$ and $\delta_2 < \delta$, it follows that both $\delta_1 \to 0$ and

$\delta_2 \to 0$ in this limit. $(R\phi)(\delta)$ may therefore be computed by replacing $\phi(\delta)$ by its Taylor expansion about the origin, namely, $(C/2)\delta^2$, with $C = \phi"(0)$. But parabolic functions are invariant under R and, hence, so is C.

The RG transformation R (4.34-4.36) preserves the monotonicity of $\phi(\delta)$. In order to see this, consider a pair of opening displacements δ and $\delta' = \lambda\delta$, with $\lambda < 1$. Let $\tilde{\phi}(\delta) = \phi(\delta_1) + \phi(\delta_2)$ for some pair of opening displacements δ_1 and δ_2 satisfying constraint (4.35). The opening displacements $\delta_1' = \lambda\delta_1$ and $\delta_2' = \lambda\delta_2$ then satisfy the similar constraint: $\delta' = \delta_1' + \delta_2'$. It therefore follows that $\tilde{\phi}(\delta') < \phi(\lambda\delta_1) + \phi(\lambda\delta_2) < \phi(\delta_1) + \phi(\delta_2) = \tilde{\phi}(\delta)$. An application of the rescaling (4.36) to both sides of this inequality finally proves the assertion.

It is easy to show that the function

$$\phi_\infty(\delta) = \min\{\frac{C}{2}\delta^2, 2\gamma\} \tag{4.37}$$

is a fixed point of R. To this end, we may distinguish the cases: a) $\delta_1 < \delta_c$ and $\delta_2 < \delta_c$; b) $\delta_1 < \delta_c$ and $\delta_2 > \delta_c$, or, equivalently, $\delta_2 < \delta_c$ and $\delta_1 > \delta_c$, and c) $\delta_1 > \delta_c$ and $\delta_2 > \delta_c$. Case (a) requires that $\delta < 2\delta_c$ and gives an unscaled energy: $\tilde{\phi}(\delta) = (C/2)(\delta/\sqrt{2})^2$. Case (b) requires that $\delta > \delta_c$. The optimal unscaled energy is obtained by taking $\delta_1 = 0$ and $\delta_2 = \delta$, with the result: $\tilde{\phi}(\delta) = 2\gamma$. Case (c) results in the unscaled energy: $\tilde{\phi}(\delta) = 4\gamma$. The function (4.37) is recovered by taking the minimum of the unscaled energies resulting from cases (a), (b) and (c) and applying the scaling (4.36) to the result.

A key question is whether the fixed point (4.37) is attractive. We have investigated this question numerically for the particular example of the UBER binding law, (4.25). Fig. 4.6 shows the evolution of ϕ_n with increasing n. It is clear from the figure that, at least for the example under consideration, the flow of functions $\phi_n(\delta)$ does indeed converge strongly to the fixed point (4.37). The relation to the asymptotic cohesive law (4.21) is as follows. We may regard $\phi_n(\delta)$ as the result of decimating and rescaling n times a cohesive layer containing $N = 2^n$ planes. The total opening displacement of the layer is obtained by undoing all the rescalings, with the result:

$\bar{\delta} = (\sqrt{2})^n \delta = \sqrt{N}\delta$. For large N, $\phi_n(\delta) \sim \phi_\infty(\delta)$ and one has

$$\bar{\phi}(\bar{\delta}) \sim \phi_\infty(\bar{\delta}/\sqrt{N}), \qquad \text{as } N \to \infty \tag{4.38}$$

which is identical to (4.21).

Equation (4.38) establishes a connection between the renormalization group, specifically as generated by transformation (4.34-4.36), and the large-N asymptotic form of the cohesive potential determined directly in the preceding Section. It is interesting to note that the RG transformations which pertain to the renormalization of interplanar potentials are markedly different from those which arise in the calculation of bulk thermodynamic properties. In this latter context, the appropriate scaling is related to the volume of the sample and is designed so as to result in well-defined extensive fields and intensive variables. In the present context, the energy densities under consideration are defined per unit area, and the limit of interest is the total energy of the cohesive layer per unit surface area, as opposed to the energy per unit volume. In addition, the independent variable of interest is the total opening displacement across the cohesive layer, as opposed to its transverse strain. These peculiarities account for the non-standard character of the renormalization group defined in the foregoing.

4.6 Summary and Conclusions

We have presented two approaches for coarse-graining interplanar potentials and determining the corresponding macroscopic cohesive laws based on energy relaxation and the renormalization group. We have analyzed the cohesive behavior of a large—but finite—number N of interatomic planes and found that the macroscopic cohesive law adopts a universal asymptotic form in the limit of large N. We have also found that this asymptotic form of the macroscopic cohesive law is an attractive fixed point of a suitably-defined renormalization-group transformation.

The universal asymptotic form of cohesive law is particularly simple: the traction rises linearly from zero to a peak stress $\bar{\sigma}_c$ at a critical opening displacement $\bar{\delta}_c$,

and subsequently drops to zero. The scaling of the peak stress and critical opening displacement is $\bar{\delta}_c \sim 1/\sqrt{N}$ and $\bar{\delta}_c \sim \sqrt{N}$. Thus, coarse-graining is accompanied by an attendant reduction (increase) in the cohesive traction (opening displacement) range, while at the same time preserving the surface of specific fracture energy of the crystal.

It is interesting to note that the size of a cohesive zone at the tip of a crack in an elastic crystal scales as $l \sim 1/\sigma_c^2$ [4]. Upon coarse-graining, the cohesive zone size increases to $\bar{l} \sim 1/\bar{\sigma}_c{}^2$, which gives $\bar{l} \sim Nl$. This scaling preserves the ratio $\bar{l}/l = \bar{d}/d$, which shows that coarse-graining has the effect of expanding the cohesive-zone size to within the resolution of the coarse-grained description. In particular, it eliminates the onerous need to resolve the atomic scale in simulations.

It is also interesting to note that the universal form of the macroscopic cohesive potential is completely determined by the constants $C = \phi''(0)$ and $\phi(\infty) = 2\gamma$. This greatly reduces the scope of the first-principles calculations required to identify the macroscopic cohesive behavior of specific materials, which can be limited to the calculation of elastic moduli, lattice constants and surface energies.

Finally, we close by suggesting possible extensions of the theory. The analysis presented in the foregoing has been restricted to symmetric (mode I) opening normal to the atomic planes. A worthwhile extension would be to consider interplanar potentials defined in terms of three opening displacements and, therefore, capable of describing tension-shear coupling. Another worthwhile extension would be to consider interplanar potentials with multiple inflection points, which would greatly enlarge the class of materials tractable within the theory.

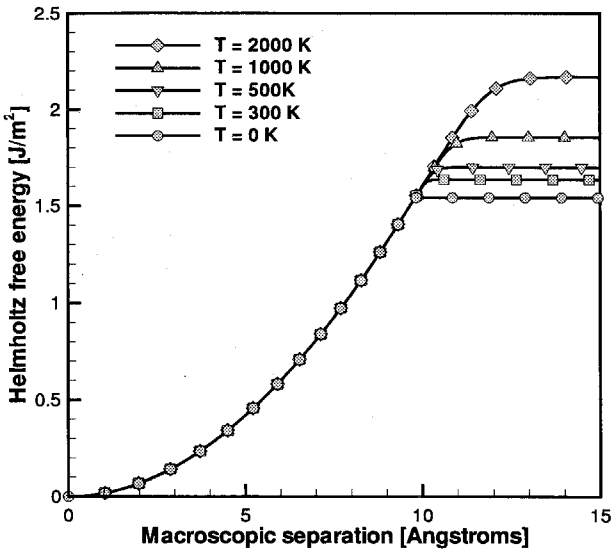

(a) Helmholtz free energy.

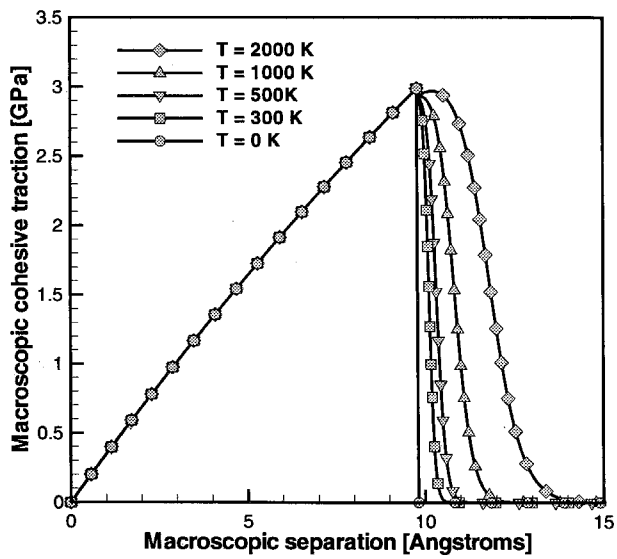

(b) Macroscopic cohesive traction.

Figure 4.5: Influence of the temperature on the effective behavior of the chain ($N = 100$).

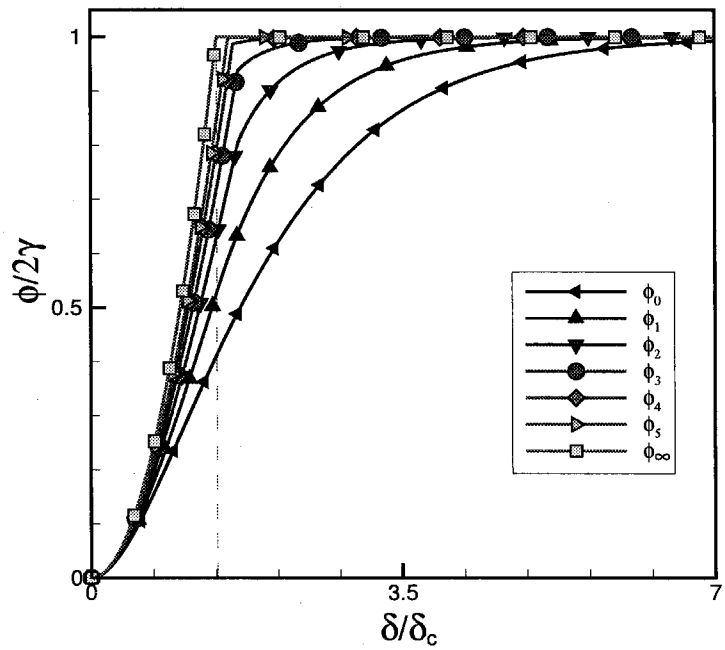

Figure 4.6: Evolution of the sequence $\phi_n,\ n = 0, 1, \ldots$ towards the *fixed point* ϕ_∞.

Chapter 5 A Cohesive Model of Stress-Corrosion Cracking

5.1 Introduction

Stress-corrosion cracking (SCC) was recognized in the nineteen fifties as an important failure mode for metallic structures subject to an aggressive environment [9]. Despite the intensive research devoted to SCC, its underlying mechanisms are yet to be fully understood and depend upon complex chemical and mechanical interactions, which vary with the environment and system studied. As a result, several models such as slip-dissolution [92, 60], film-induced cleavage [82, 83] and hydrogen embrittlement [85, 52] were suggested as potential mechanism for SCC. These models, each consistent with experimental data in particular systems, suggest SCC cannot be explained by a universal mechanism [87, 66]. We focus our attention to systems where hydrogen embrittlement is recognized to be the principal source of damage for the material, e.g., high-strength steel in aqueous environments [43].

Hydrogen embrittlement is often described as a two-step process. During the first step, the hydrogen is absorbed from the environment into the host metal and diffuses through the metal lattice toward a critical region in the material, e.g., at the vicinity of a crack tip [87, 48]. The diffusion process is driven by the gradient of the chemical potential of the hydrogen [42] and depends on the state of stress in the metal. As the hydrogen diffuses in the metal, it influences the plastic behavior of the material. Several authors have reported either softening or hardening of the material (see [87] for a brief review). In addition to lattice diffusion, the hydrogen can be transported via pipe-diffusion but evidences show that this mode of transportation could be neglected [45, 26, 87]. Several other authors have suggested as well the possibility of trapping sites in the metal impeding the hydrogen diffusion [87]. During the second step,

the hydrogen lowers the specific fracture energy or critical energy release rate of the material, eventually leading to the advance of the crack.

We propose in this chapter to consider both phases of hydrogen embrittlement in order to define a model of SCC with quantitative predicting ability with regard to the life of specimens in an aggressive environment. The first step will be approached by using a stress-assisted diffusion equation. Our approach to the second step is to use the concepts developed in chapter 4, in conjunction with a thermodynamic framework suggested by Rice *et al.* [80], in order to account for the deleterious effect of hydrogen on the fracture properties of the material. In Section 5.2, we derive a cohesive law function of the impurity concentration. In Section 5.3, we consider the stress-assisted diffusion of segregants into the host metal. Section 5.4 describes the implementation of our model in the finite element framework. Finally, in Section 5.5, we validate our model by comparison with experiments available in the literature.

5.2 Cohesive Law in the Presence of Impurities

We describe the fracture process by means of an irreversible cohesive law which has the important characteristic of being a function of the impurities concentration present in the material. In this manner, we account for a possible embrittling effect of segregants in the host metal. The chemistry-dependent cohesive law is based on the universal macroscopic cohesive law developed in chapter 4 and is defined as

$$\sigma(\delta) = \begin{cases} \bar{C}\delta, & \text{if } \delta < \delta_c \\ 0, & \text{otherwise} \end{cases} \tag{5.1}$$

with

$$\bar{C} = \frac{C}{N} \tag{5.2}$$

$$\delta_c = 2\sqrt{\frac{\gamma}{\bar{C}}} \tag{5.3}$$

$$\sigma_c = 2\sqrt{\bar{C}\gamma} \tag{5.4}$$

where C is a simple function of the elastic moduli of the material, as defined by equation 4.3; δ_c is the critical value of the opening displacement beyond which the cohesive stress drops suddenly to zero; and σ_c is the peak value of the cohesive stress occurring at $\delta = \delta_c$.

It is worthwhile to note that both δ_c and σ_c are function of the surface energy of the material while C depends solely on its elastic properties. We postulate that the impurities present in the material will have a much greater influence on its surface energy than its elastic properties. In that case, C will not depend on the presence of impurties in the material and is a constant. What remains to be determined is the functional dependence of the surface on the impurity concentration. This will be discussed in Subsection 5.2.2.

Another important point to make is that the universal cohesive law defined by equation 5.1 contains the elastic contribution of the cohesive layer. The use of the continuum mechanics to model the bulk of the material already takes this contribution into account. Therefore, one should correct the cohesive law so as to remove its contribution to the elastic energy. We investigate that issue in the next Subsection.

5.2.1 Elastically Corrected Cohesive Law

The cohesive law has to be modified in order to remove the elastic contribution resulting from the renormalization of the interplanar atomic potential. We define the modified cohesive law $t(\delta)$ as follows:

$$t(\delta) = \sigma(\delta + \frac{t(\delta)}{\sigma'(0)}) \tag{5.5}$$

It has the effect of skewing the cohesive law so as to give an infinite slope at the origin. One obtains (see appendix A) the following elastically corrected cohesive law:

$$t(\delta) = \begin{cases} \sigma_c - \bar{C}\delta, & \text{if } \delta < \delta_c \\ 0, & \text{otherwise} \end{cases} \tag{5.6}$$

Therefore, we recover the classic linearly decreasing cohesive law by correcting the universal macroscopic cohesive law, as illustrated in figure 5.1.

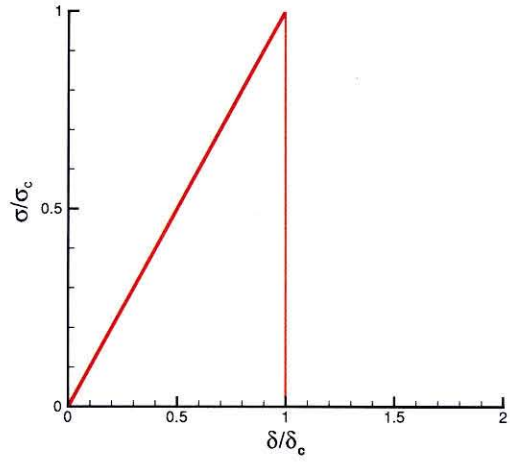

(a) Universal cohesive law.

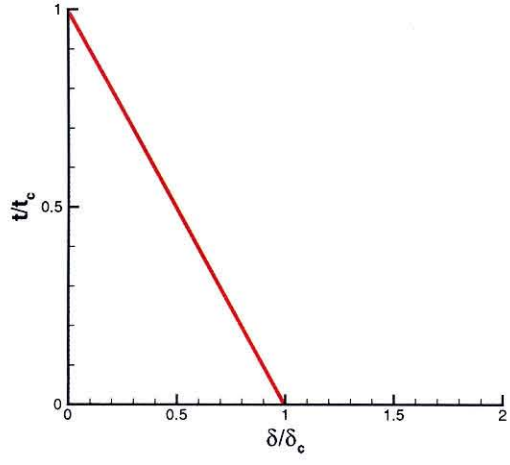

(b) Elastically Corrected cohesive law.

Figure 5.1: Universal macroscopic cohesive law and its elastic correction.

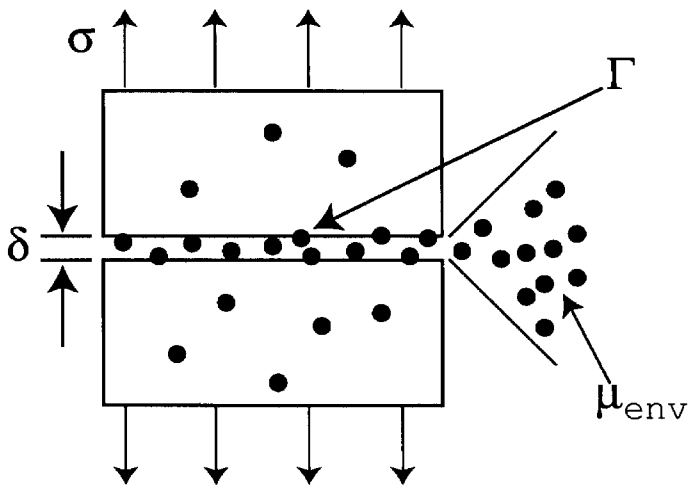

Figure 5.2: Thermodynamic interface ([80]).

5.2.2 Surface Energy as a Function of Impurity Concentration

In this Section, we briefly summarize the results obtained by [80] and, in particular, the functional dependence of the surface energy as a function of the impurity concentration. In [80], the authors considered the fracture process to take place along a thermodynamic interface depicted in figure 5.2. The interface is defined by two surfaces S^+ and S^- which are separated by a distance δ called opening displacement. δ is assumed to be equal to zero prior to separation. In addition, impurities can be present on the two surfaces of the interface at all times. They can be associated with well-defined concentrations Γ^+ and Γ^- defined per unit area, in excess of those of the bulk phases. The concentration on the interface Γ is equal to the sum of Γ^+ and Γ^-. The interface is in contact with an external environment characterized by a known chemical potential μ^{env}. All thermodynamic functions relevant to the interface are functions solely of the temperature T, the opening displacement δ and the interface concentration Γ. The infinitesimal change of the interface's internal energy is equal

to

$$du = Tds + \sigma d\delta + \mu d\Gamma \tag{5.7}$$

where u is the excess internal energy of the interface, s the excess entropy of the system, σ the cohesive traction on the interface and μ its chemical potential. By assuming the temperature to be constant, it is more convenient to work in terms of the excess Helmholtz free energy $f(\delta, \Gamma) = u - Ts$.

$$df = \sigma d\delta + \mu d\Gamma \tag{5.8}$$

This relation is assumed to hold during the separation of the interfaces. If the functional expression for f were known as a function of δ and Γ, we could immediately determine the cohesive traction σ as a function of δ and Γ since

$$\frac{\partial f(\delta, \Gamma)}{\partial \delta}|_{\Gamma} = \sigma(\delta, \Gamma) \tag{5.9}$$

Instead, additional assumptions have to be made in order to obtain $\sigma(\delta, \Gamma)$. The first one, suggested by [80], is to assume that $f(\delta, \Gamma)$ has two limiting values

$$\lim_{\delta \to 0} f(\delta, \Gamma) = f_b(\Gamma) \tag{5.10}$$

$$\lim_{\delta \to \infty} f(\delta, \Gamma) = f_{fs}(\Gamma^+) + f_{fs}(\Gamma^-) \tag{5.11}$$

The interpretation of these two limits is straightforward. When δ is equal to zero, the interface can be viewed as a grain boundary in the metal. In that case, f_b is the free energy of a grain boundary. When δ goes to infinity, the interface becomes two free surfaces so that $f(\delta, \Gamma)$ is equal to the sum of the two free surfaces free energy f_{fs}.

If separation is fast enough to be at constant interfacial concentration Γ, the work of separation of the interface $2\gamma_{int}$ is found to be equal to

$$(2\gamma_{int})_{\Gamma=const} = (2\gamma_{int})_{\Gamma=0} - \int_0^{\Gamma} \{\mu_b(\Gamma) - \mu_{fs}(\frac{\Gamma}{2})\} d\Gamma \tag{5.12}$$

Assuming the surface coverage is not saturated [80], the Langmuir-McLean model can

be adopted so that

$$\mu_i(\Gamma) = \Delta g_i^0 + RT \ln\{\frac{\Gamma}{\Gamma_i^s - \Gamma}\} \tag{5.13}$$

where the index i refers to a grain boundary or a free surface and Γ_i^s is the surface concentration at saturation (full coverage). According to [80], when combined with equation 5.13, equation 5.12 can be simplified to

$$(2\gamma_{int})_{\Gamma=const} \approx (2\gamma_{int})_{\Gamma=0} - \Delta g\ \Gamma \tag{5.14}$$

where Δg stands for $\Delta g_b - \Delta g_s$. This is the relation we adopt in our model of stress-corrosion cracking.

5.2.3 Effect of the Impurities on the Cohesive Law

Combining equations 5.14 and 5.6, we obtain the final expression of the chemistry-dependent cohesive law:

$$\sigma(\delta, \Gamma) = \begin{cases} 2\sqrt{\bar{C}[(\gamma_{int})_{\Gamma=0} - \Delta g/2\ \Gamma]} - \bar{C}\delta, & \text{if } \delta < \delta_c \\ 0, & \text{otherwise} \end{cases} \tag{5.15}$$

The critical opening displacement and cohesive stress become respectively

$$\delta_c(\Gamma) = 2\sqrt{\frac{(\gamma_{int})_{\Gamma=0} - \Delta g/2\ \Gamma}{\bar{C}}} \tag{5.16}$$

and

$$\sigma_c(\Gamma) = 2\sqrt{\bar{C}[(\gamma_{int})_{\Gamma=0} - \Delta g/2\ \Gamma]} \tag{5.17}$$

The influence of the reduction of the surface energy due to the presence of the impurites on the cohesive law is shown in figure 5.3. $2\gamma_0$ is the surface energy of the material free of impurities.

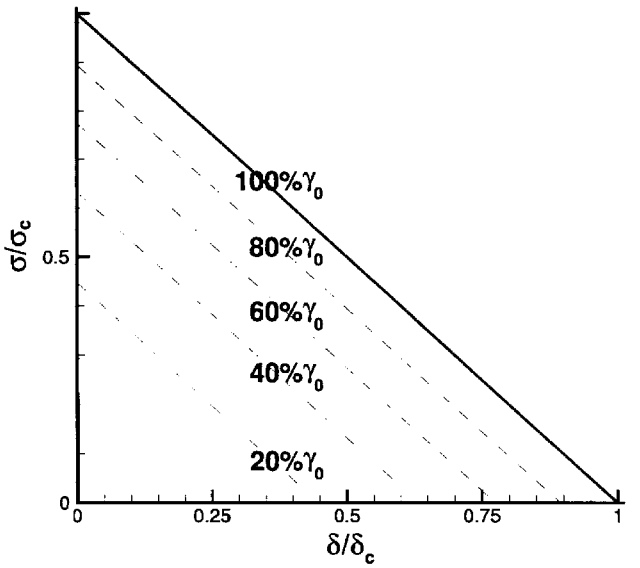

Figure 5.3: Dependence of the cohesive law on the impurities concentration.

5.3 Impurity Stress-Assisted Diffusion

The governing equation for hydrogen diffusion is formulated as a stress-assisted diffusion initial-boundary value problem (IBVP). We consider the system impurity/host metal to be an ideal (dilute) solid solution. The impurity in the lattice is modeled as a point defect causing dilatational distortion only. Its chemical potential can be written as

$$\mu(C, T, \boldsymbol{\sigma}) = \mu^0 + RT \ln C - p\bar{V} \tag{5.18}$$

where C is the concentration of the diffusing species, R is the gas constant equal to 8.314 $J/Kmol$, T is the absolute temperature, p is the hydrostatic stress equal to $\sigma_{kk}/3$ and $\bar{V}$ is the partial molar volume of hydrogen in solid solution. The flux of hydrogen is related to the hydrogen chemical as follows [73]:

$$\mathbf{J} = -MC\nabla\mu \tag{5.19}$$

where M is the mobility of the segregant. Replacing equation 5.18 into equation 5.19 and using the ideal solution assumption, we obtain (after some algebra)

$$\mathbf{J} = -D\nabla C + \frac{D\bar{V}}{RT} C \nabla p \tag{5.20}$$

where D is the lattice diffusion constant. Although D is a function of the temperature and the amount of dislocations present in the material, we keep it constant as a first approximation. $\bar{V}$ is assumed to be constant as well. The conservation equation for the segregant is

$$\frac{\partial C}{\partial t} + \nabla \cdot \mathbf{J} = 0 \tag{5.21}$$

By inserting equation 5.20 into equation 5.21, we have

$$\frac{\partial C}{\partial t} = DC_{,ii} - \frac{D\bar{V}}{RT} C_{,i} p_{,i} - \frac{D\bar{V}}{RT} C p_{,ii} \tag{5.22}$$

In order to have a well-defined problem, we must specify the proper set of initial and boundary conditions. We impose either a value for the concentration along the crack flanks or a mixed type boundary condition expressed as follows:

$$\frac{\delta}{\delta_c} D_n C + (1 - \frac{\delta}{\delta_c})\ \mathbf{J} \cdot \mathbf{n} = \frac{\delta}{\delta_c} D_n C_{eq} \tag{5.23}$$

where D_n is an adjustable normal diffusion constant, n is the external normal to the crack flank, and C_{eq} is a given (equilibrium) concentration determined from the external environment. The mixed type boundary condition is enforced on the boundary of the crack flanks at the vicinity of the crack tip.

We justify the use of a mixed boundary condition as follows. Far away from the crack tip, equilibrium conditions are attained. The concentration of the impurities along the crack flanks is equal to the equilibrium concentration as dictated by the external environment. At the crack tip, the opening displacement is zero so that impurities from the external environment are prevented from penetrating into the bulk of the metal. In other words, the (normal) flux of impurities at the crack tip is

zero. In-between, there is a region which is neither in equilibrium nor isolated from the environment. We postulate that, in that region, the normal flux is proportional to the difference between the equilibrium concentration and the actual concentration on the crack flank. Consistency of the mixed type boundary conditions with the ones at the crack tip and far way from it is achieved by the dependence of the mixed type boundary condition on δ. The location along the crack flank at which equilibrium is attained is chosen to be where δ attains its critical value, i.e., outside of the active cohesive zone.

The stress-assisted diffusion problem can now be formulated as follows:

$$\begin{cases} \frac{\partial C}{\partial t} = DC_{,ii} - \frac{D\bar{V}}{RT}C_{,i}p_{,i} - \frac{D\bar{V}}{RT}Cp_{,ii}, & \text{in } B \\ \\ \frac{\delta}{\delta_c}D_nC + (1 - \frac{\delta}{\delta_c})\,\mathbf{J}\cdot\mathbf{n} = \frac{\delta}{\delta_c}D_nC_{eq}, & \text{on } \partial B_m \\ \\ C = C_{eq}, & \text{on } \partial B_C \end{cases} \tag{5.24}$$

where B is the domain of interest, ∂B_C, the boundary where a concentration is prescribed and ∂B_m, the boundary where a combination of the normal flux and the concentration is prescribed. The initial value of C is taken to be zero everywhere except on ∂B_C where it is equal to C_{eq}.

5.4 Coupling Mechanics with Chemistry

In this Section, we formulate the coupled initial boundary value problem defined by the mechanical boundary value problem and the stress-assisted diffusion initial boundary value problem.

This IBVP depends on the mechanical fields through the boundary conditions and the stress-term present in the partial differential equation. In the applications of interest here, the change in the mechanical fields are very slow in time so that dynamic effects are not relevant. The inertia forces and strain hardening effects can therefore

be neglected and it suffices to solve the static mechanical equilibrium equations.

$$\begin{cases} \nabla \cdot \boldsymbol{\sigma} &= 0, \quad \text{in } B \\ \boldsymbol{\sigma} \cdot \mathbf{n} &= \mathbf{t}, \quad \text{on } \partial B_t \\ \mathbf{u} &= \bar{\mathbf{u}}, \quad \text{on } \partial B_u \end{cases} \tag{5.25}$$

where $\boldsymbol{\sigma}$ is the stress tensor, $\mathbf{t}$, the applied tractions, $\bar{\mathbf{u}}$, the prescribed displacement field and $\mathbf{n}$, the outward normal of the domain boundary. The dependence of the mechanical equations on the impurities is implicitly present in the material constitutive equations. The presence of impurities may affect the material fracture toughness.

The constitutive model adopted for the material behavior follows the J-2 flow theory of plasticity with isotropic-hardening. We adopt the following conventional power hardening law

$$\sigma_y = \sigma_{y0}(1 + \frac{\epsilon^p}{\epsilon_0^p})^{\frac{1}{n}} \tag{5.26}$$

5.4.1 Finite Element Discretization

Static equilibrium is enforced weakly by recourse to the virtual work principle

$$\int_B \boldsymbol{\sigma} : \nabla \boldsymbol{\eta} \; dB = \int_{\partial B_t} \mathbf{t} \cdot \boldsymbol{\eta} \; dS \tag{5.27}$$

where $\boldsymbol{\eta}$ is an admissible virtual displacement field. Upon a finite element discretization of equation 5.27, the governing equations become

$$\mathbf{f}^{int} = \mathbf{f}^{ext} \tag{5.28}$$

where $\mathbf{f}^{ext}$ is the external force array which accounts for the applied surface tractions and $\mathbf{f}^{int}$, the internal force array arising from the current state of stress. The system of non-linear equations is solved by recourse to a Newton-Raphson iteration scheme.

The weak form of the stress-assisted boundary value problem is

$$\int_B \dot{C} \; \eta \; dB = \int_B \mathbf{J} \cdot \nabla \eta \; dB - \int_{\partial B} \mathbf{J} \cdot \mathbf{n} \; \eta \; dS \tag{5.29}$$

where η is an admissible virtual concentration field. Using equation 5.23, we obtain

$$\int_B \dot{C}\ \eta\ dB = \int_B \mathbf{J}\cdot\nabla\eta\ dB + \alpha(\delta)\int_{\partial B_m}\eta\ dS + \beta(\delta)\int_{\partial B_m} C\eta\ dS \tag{5.30}$$

where

$$\begin{cases} \alpha(\delta) = -\frac{C_{eq}}{1-\delta/\delta_c} \\ \beta(\delta) = \frac{\delta/\delta_c}{1-\delta/\delta_c} \end{cases}$$

The finite element discretization of equation 5.30 gives the semi-discrete system of equations

$$\mathbf{M}\dot{\mathbf{C}} + \mathbf{K}\ \mathbf{C} = \mathbf{Q} \tag{5.31}$$

where $\mathbf{M}$ is the concentration capacity matrix, $\mathbf{C}$ is the array of nodal concentrations, $\mathbf{K}$ is the diffusivity matrix and $\mathbf{Q}$ is the diffusion flux array. In indicial notation, we have

$$\begin{aligned} [\mathbf{M}]_{ab} &= \textstyle\int_B N_a N_b\ dB \\ \{\mathbf{Q}\}_a &= \alpha(\delta)\textstyle\int_{\partial B} N_a\ dS \\ [\mathbf{K}]_{ab} &= [\mathbf{K_1}]_{ab} + [\mathbf{K_2}]_{ab} \end{aligned}$$

with

$$\begin{aligned} [\mathbf{K_1}]_{ab} &= \textstyle\int_B \{D\ \nabla N_a\cdot\nabla N_b - \frac{D\Delta V}{RT}\nabla p\cdot\nabla N_a\ N_b\}\ dB \\ [\mathbf{K_2}]_{ab} &= -\beta(\delta)\textstyle\int_{\partial B_m} N_a N_b\ dS \end{aligned}$$

The critical stable time step of our problem is determined solely by the diffusion equation. In the applications of interest, the relevant time scale is much bigger than the critical time step so that we integrate the diffusion equation implicitly by the generalized trapezoidal rule, with the result

$$\begin{cases} \mathbf{M}\dot{\mathbf{C}}_{n+1} + \mathbf{K}\mathbf{C}_{n+1} &= \mathbf{Q}_{n+1} \\ \mathbf{C}_{n+1} &= \mathbf{C}_n + \Delta t\ \dot{\mathbf{C}}_{n+\alpha} \\ \dot{\mathbf{C}}_{n+\alpha} &= (1-\alpha)\dot{\mathbf{C}}_n + \alpha\dot{\mathbf{C}}_{n+1} \end{cases} \tag{5.32}$$

where alpha is a real number in $(0, 1]$ and Δt the time step.

The coupling of the mechanical and stress-assisted diffusion equations is handled by means of a staggered procedure. Given an initial distribution of impurities, a

mechanical step is computed assuming the impurities distribution to remain constant. The resulting mechanical fields are in-turn held constant and used to solve the stress-assisted diffusion equation. The computed segregant concentration distribution is then used as the initial conditions for the next time step, completing one time-stepping cycle.

5.5 Numerical Simulation of the Static Fatigue Test

Static fatigue tests have been extensively used in the past to investigate the affinity of specific materials to stress-corrosion cracking in various environments. These tests can therefore serve as a benchmark to assess the predictive ability of the model developed in the foregoing.

The aim of such tests is to determine the value of K_{Iscc}, the initial stress-intensity factor below which stress-corrosion cracking is not observed. K_{Iscc} can be found by applying a decreasing series of initial K_I until the specimen does not break. The first value of K_I in the series is usually chosen slightly below the critical stress-intensity factor K_{Ic}.

5.5.1 Steel in Artificial Sea-Water

In their experiments [6], Beachem and Brown tested several center-cracked specimens in plane strain conditions. The material used was AISI 4340 steel. After being loaded to the selected stress, the center cracked portions of the specimens were immersed in a 3.5 percent sodium chloride solution. After recording the time to failure of each specimens, the authors inferred a K_{Iscc} value of 12 $ksi\sqrt{in}$.

The center crack panel, shown in figure 5.4, is subject to a constant tensile loading normal to the plane of the crack. The environment is enclosed in the crack and is allowed to attack the metal through the specimen's crack faces. Tables 5.1 and 5.2 summarize the material parameters used in our numerical simulations. We obtained them from [6, 87, 94].

The experimental results are summarized in table 5.3. The stress-intensity factors

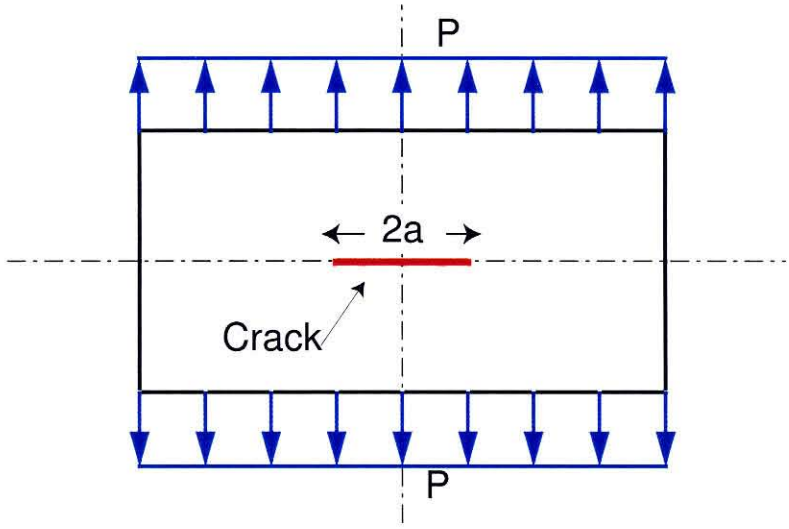

Figure 5.4: Case study.

Material Parameters					
E [GPa]	ν	σ_y [MPa]	ϵ_0^p	n	K_{Ic} [MPa$\sqrt{\text{m}}$]
210	0.3	1600	10^{-4}	8	96.8

Table 5.1: Mechanical material constants.

Material Parameters				
D	V_H	V_M	Δg	Γ_s
$[m^2/s]$	$[m^3/mol]$	$[m^3/mol]$	$[kJ/mol]$	$[mol/m^2]$
$1.33\ 10^{-8}$	2.10^{-6}	$7.116\ 10^{-6}$	44	$2.65\ 10^{-5}$

Table 5.2: Diffusion material constants.

reported in the table were computed from the following equation:

$$K_I = P\sqrt{\pi a} f(\frac{2a}{W}) \tag{5.33}$$

with

$$f(\frac{2a}{W}) = \sqrt{\sec\frac{\pi a}{2W}}[1 - 0.025(\frac{a}{W})^2 + 0.06(\frac{a}{W})^4]$$

where P is the applied stress, $2a$ is the crack length and W, the specimen width. In order to compare the experimental data shown in table 5.3, we ran several simulations for different values of constant applied stress while maintaining the environment unchanged. The temperature is assumed to remain constant throughout the calculations and set to $300K$. Since the equilibrium concentration of hydrogen was not given, we determined it from a similar experiment where the authors measured a

Center-Cracked Specimens				
K_I	Time	Width	Crack Length	Load
$[ksi\sqrt{in.}]$	$[min.]$	$[in.]$	$[in.]$	$[lb]$
88.5	...	1.473	0.750	12,150
85.0	...	1.499	0.598	15,000
37.1	84	1.503	0.587	6,500
27.2	399	1.493	0.617	4,630
25.0	2452	1.499	0.600	4,330
19.1	4464	1.500	0.617	3,150
14.6	27024	1.508	0.640	2,460
14.2	54545	1.473	0.740	1,970

Table 5.3: Summary of Experimental Data ([6]).

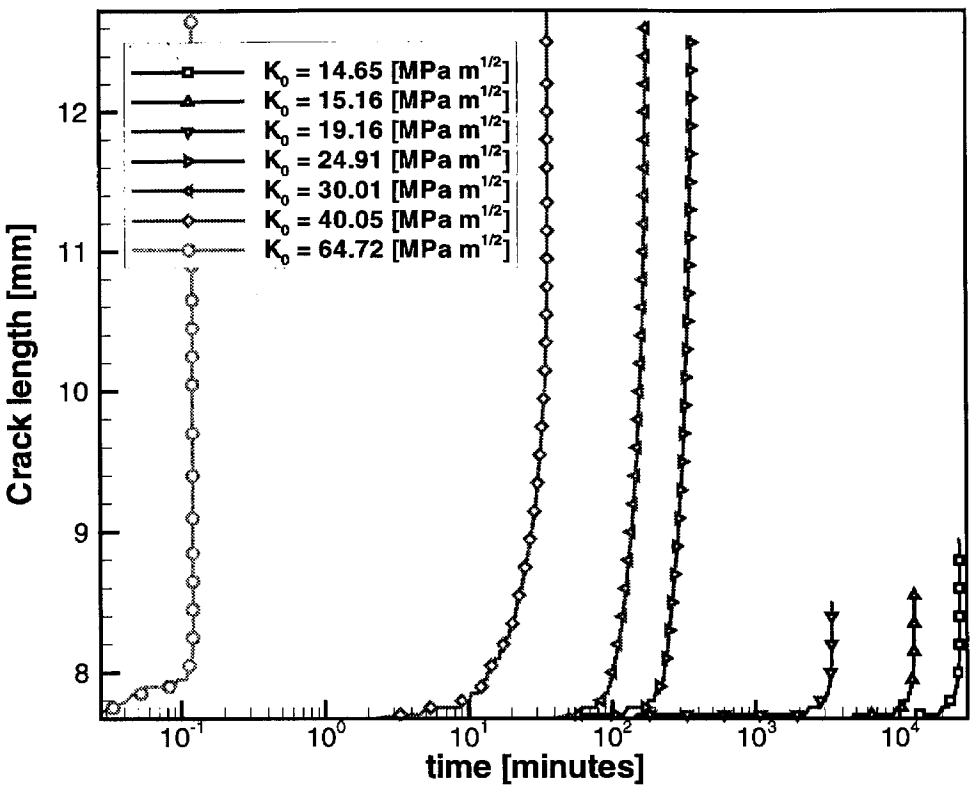

Figure 5.5: Crack length as a function of time.

C_0 of 0.1 (ppm wt) under the same conditions of the original experiment [28]. The adjustable normal diffusion constant D_n in equation 5.23 was set to 3.5 $10^{-8} m^2/s$.

We recorded the crack length as a function of time (figure 5.5) and were able to estimate the time-to-failure by determining the time at which the crack reaches the unstable regime, i.e., when the growth rate goes to infinity. The resulting time-to-failure compared with the experimental data are shown in figure 5.6. The squares are the numerical results and the triangles are the experimental results. The two compare well even though it appears that our numerical result does not reach a limiting value of for K_{Iscc}. In fact, it is not clear if K_{Iscc} can really be defined without the corresponding time after which a specimen is considered never to fail. If a specimen hasn't failed

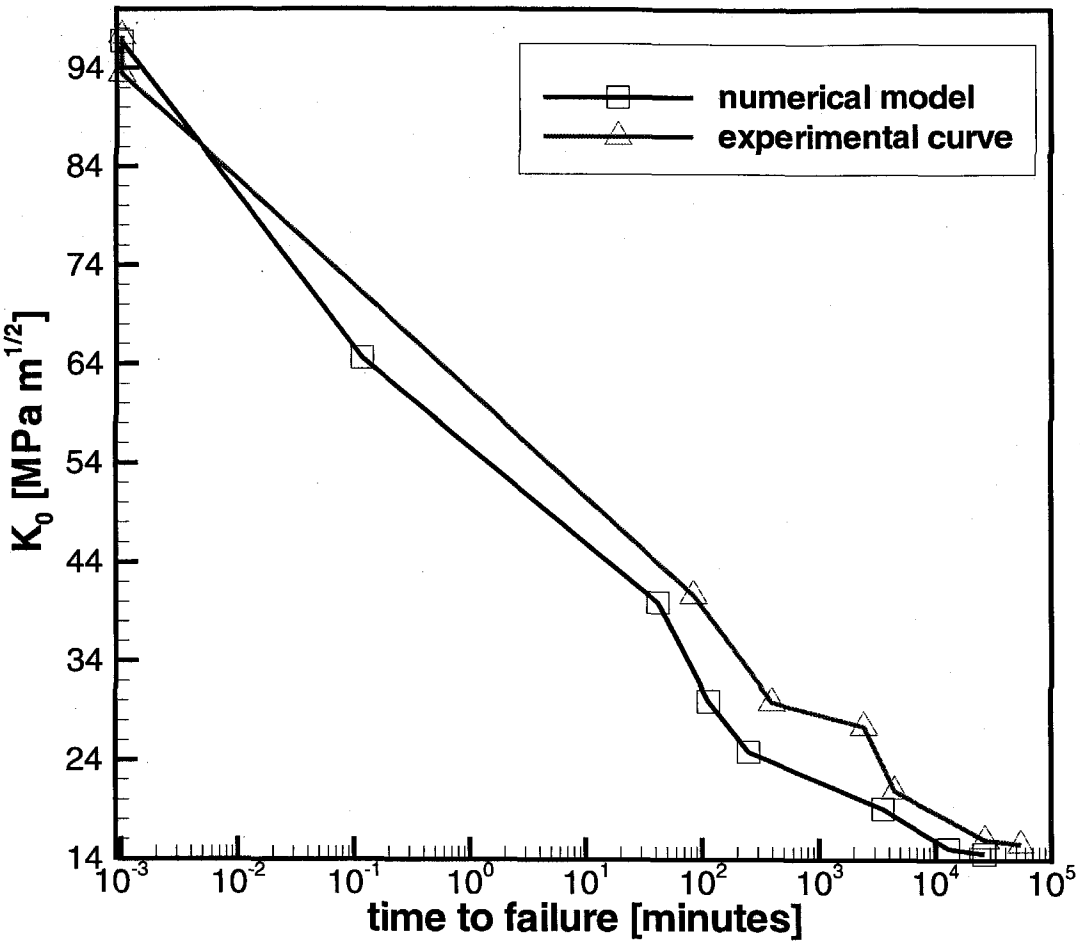

Figure 5.6: Comparison of the experimental times to failure with the numerical ones.

after that critical time, the experiment is stopped and the time to failure is considered to be equal to infinity. However, if one could wait long enough, the specimen might fail. This is what we observe in our simulations. Although we do not reach a limiting value for K_{Iscc}, the time to failure becomes very large and comparable to the critical amount of time after which experimentalists consider the specimen not to fail.

Material Parameters					
E [GPa]	ν	σ_y [MPa]	ϵ_0^p	n	K_{Ic} [MPa$\sqrt{\text{m}}$]
200	0.3	1300	10^{-4}	8	62

Table 5.4: Mechanical material constants (AISI-4130 Steel).

5.5.2 Steel in Hydrogenous Gas

In this Section, we investigate the delayed fracture of high strength steels in gaseous hydrogen atmosphere. The material is a high strength steel of the type AISI-4130. The material parameters are summarized in table 5.4. The specimen were immersed in a gaseous environment in contact with the metal. The equilibrium concentration for the hydrogen atom is given (in ppm wt) by Sievert's law

$$C_0 = \alpha \sqrt{p_{H_2}} \tag{5.34}$$

where α is 3.6 10^{-3} [27] at room temperature (300K) and p_{H_2} is the hydrogen pressure in $[kPa]$. This gives a C_0 of 6.5 10^{-2} (ppm wt). In [58], the crack velocity was measured as a function of the stress intensity factor for a hydrogen pressure of 77kPa; see figure 5.7. On that same figure, the numerical rate of crack growth is shown as a red line. Although the numerical crack propagation rate seems to be continuous (figure 5.7), the crack advances intermittently. The controlling process is the rate of hydrogen absorption and diffusion. When the hydrogen attains a critical concentration, the cohesive zone weakens to the point that the crack advances. The crack stops when it encounters a region poor enough in hydrogen content. The process repeats itself as the hydrogen continuously diffuses toward the crack tip. Figure 5.5.2 illustrates this process. Four snapshots of the hydrogen concentration contour plot are shown. The orange segments are the boundary of the specimen. The color red represents a concentration equal to the equilibrium concentration and the blue one represents a concentration equal to zero.

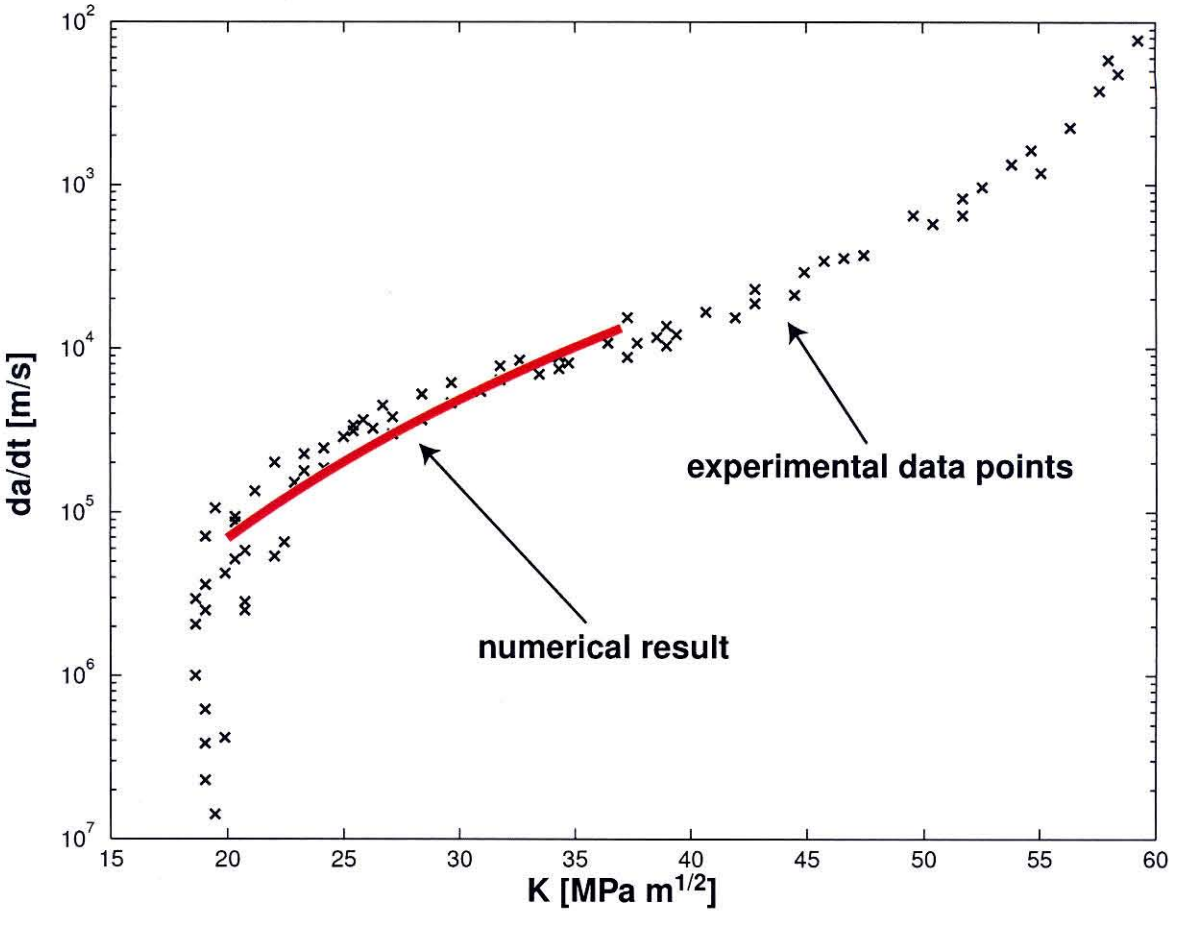

Figure 5.7: Crack velocity as a function of the applied stress intensity factor [27].

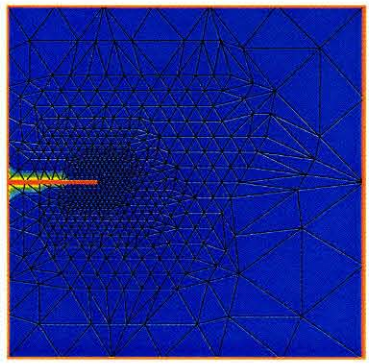

(a) t=0 hour.

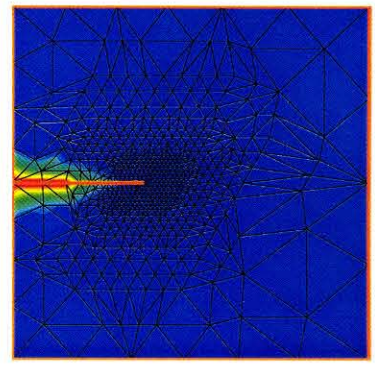

(b) t=100 hours.

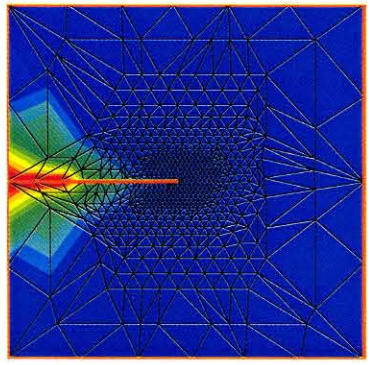

(c) t=500 hours.

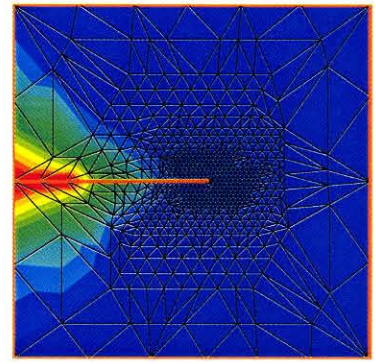

(d) t=1000 hours.

Figure 5.8: Snapshots of the hydrogen concentration distribution in the specimen. The crack grows intermittently and away from the region of high hydrogen content.

5.6 Summary and Conclusions

We have derived a finite-element model of stress-corrosion cracking with quantitative predicting ability with regard to the life of specimen in an aggressive environment. The principal mechanism of damage considered was hydrogen embrittlement. Hydrogen transport was modeled by a stress-assisted diffusion equation including the hydrostatic stress terms. The kinetics of hydrogen absorption was accounted for by

a mixed-type boundary condition in the region close to the crack tip. The hydrogen-induced reduction of the material cohesive energy was determined by the use of cohesive theories of fracture. We derived a cohesive law which exhibits a dependence on the hydrogen concentration.

Our simulations show close agreement with experimental data observed in "static" fatigue load tests. The crack propagation observed in our simulation is intermittent and driven by the hydrogen absorption and diffusion. As the hydrogen reaches a critical distribution in the fracture process zone, the material fails and the crack propagates until it reaches a zone poorer in hydrogen. If the zone with depleted hydrogen offers enough resistance against the propagation of the crack, the crack eventually arrests. As the hydrogen continues to diffuse toward the crack tip, this process repeats itself, leading to intermittent crack growth until complete failure of the structure.

Chapter 6 Conclusions

We have investigated the use of cohesive theories of fracture for the purpose of studying fatigue crack propagation and stress-corrosion cracking. The fatigue model derived in the first part of this dissertation relies on a cohesive law which has the distinguishing characteristic of exhibiting unloading-reloading hysteresis. The inclusion of unloading-reloading hysteresis into the cohesive law simulates dissipative mechanisms such as crystallographic slip and frictional interactions between asperities, and the accumulation of damage within the cohesive zone, eventually leading to complete decohesion and crack extension. It has also the important consequence of preventing shakedown, thus allowing for steady crack growth. In addition, the model is free from any small-scale yielding assumptions as a consequence of the explicit resolution of the plastic fields and cohesive lengths. In particular, it does not directly rely on the stress-intensity factor as a crack-tip loading parameter. Our calculations demonstrated that the model is capable of a unified treatment of long cracks under constant-amplitude loading, short cracks and overloads. In the case of long cracks and constant-amplitude loads, the theory predicted Paris-like behavior. By way of contrast, the same theory predicts qualitatively the experimentally observed growth acceleration in the short-crack regime and the equally observed growth retardation due to overloads, without *ad hoc* corrections or tuning.

We have also derived a model of fatigue initiation, based on the hysteretic cohesive law developed for the fatigue crack propagation model. The monotonic cohesive envelope used was of the UBER type, corrected to have an infinite slope at the origin. The S-N curves obtained from the model showed reasonable agreement with the experimental data for different types of metals. The model captured the effect of the mean-stress, at least qualitatively. Its simplicity makes it an ideal candidate for a larger scale framework in order to study more complex problems such as the environmental, temperature, as well as multi-axial loading effect on fatigue nucleation.

In the second part of this work, we have presented two approaches for coarse-graining interplanar potentials and determined the corresponding macroscopic cohesive laws based on energy relaxation and the renormalization group. We have analyzed the cohesive behavior of a large—but finite—number N of interatomic planes and found that the macroscopic cohesive law adopts a universal asymptotic form in the limit of large N. We have also found that this asymptotic form of the macroscopic cohesive law is an attractive fixed point of a suitably-defined renormalization-group transformation. Coarse-graining is accompanied by an attendant reduction (increase) in the cohesive traction (opening displacement) range, while at the same time preserving the surface of specific fracture energy of the crystal. It also has the effect of expanding the cohesive-zone size to within the resolution of the coarse-grained description. In particular, it eliminates the onerous need to resolve the atomic scale in simulations. In addition, the scope of the first-principles calculations required to identify the macroscopic cohesive behavior of specific materials can be limited to the calculation of elastic moduli, lattice constants and surface energies.

The coarse-grained macroscopic law was then used to develop a model of stress-corrosion cracking. The principal mechanism of damage considered was hydrogen embrittlement. Hydrogen transport was modeled by a stress-assisted diffusion equation including the hydrostatic stress terms. The kinetics of hydrogen absorption was accounted for by a mixed-type boundary condition in the region close to the crack tip. The material surface energy is reduced due to the presence of hydrogen in the metal according to a thermodynamic relation given by [80]. This relation was used directly in the coarsed-grained cohesive law. In particular, we were able to determine the functional dependence of the parameters of the cohesive law—i.e., the critical cohesive stress and critical opening displacement—without any additional assumptions. Our simulations show close agreement with experimental data observed in "static" fatigue load tests. The crack propagation observed in our simulation is intermittent and driven by the hydrogen absorption and diffusion. As the hydrogen reaches a critical distribution in the fracture process zone, the material fails and the crack propagates until it reaches a zone poorer in hydrogen. If the zone with depleted hydrogen offers

enough resistance against the propagation of the crack, the crack eventually arrests. As the hydrogen continues to diffuse toward the crack tip, this process repeats itself, leading to intermittent crack growth until complete failure of the structure.

Finally, we close by suggesting possible improvements of the different models proposed here. The analysis presented in this work has been restricted to symmetric (mode I) opening normal to the plane of the crack. A worthwhile extension would be to consider cohesive laws defined in terms of three opening displacements, and therefore capable of describing tension-shear coupling. Another worthwhile extension to the coarse-graining approach would be to consider interplanar potentials with multiple inflection points, which would greatly enlarge the class of materials tractable within the theory. Finally, it would be of great interest to couple the model of fatigue crack growth and stress-corrosion cracking to study corrosion fatigue for several systems metal/environment under various conditions of loading.

Appendix A Derivation of the Elastically Corrected Cohesive Law

We modify the universal cohesive law in order to remove its elastic contribution. The universal cohesive law is defined as

$$\sigma(\delta) = \begin{cases} \bar{C}\delta, & \text{if } \delta < \delta_c \\ 0, & \text{otherwise} \end{cases} \tag{A.1}$$

We define the modified (corrected) cohesive law $t(\delta)$ as follows:

$$t(\delta) = \sigma(\delta + \frac{t(\delta)}{\sigma'(0)}) \tag{A.2}$$

where here and subsequently, a prime denotes differentiation of a function of a single variable. It has the effect of skewing the cohesive law so as to give an infinite slope at the origin. From equation A.2 and equation A.1, we have

$$t'(\delta) = \sigma'(\eta)(1 - \frac{\sigma'(\eta)}{\bar{C}})^{-1} \tag{A.3}$$

where η is equal to $\delta + \frac{t(\delta)}{\sigma'(0)}$. In order to determine the expression of $t(\delta)$, we consider the three cases, namely: $\eta > \delta_c$, $\eta < \delta_c$ and $\eta = \delta_c$.

Case $\eta > \delta_c$

If $\eta > \delta_c$, then $\sigma(\eta) = 0$ and equation A.2 yields $t(\delta) = 0$. Therefore, from the definition of η, we have $\delta > \delta_c$.

Case $\eta < \delta_c$

If $\eta < \delta_c$, then $t'(\delta) = \infty$ as a direct result of equation A.3. From equation A.2, $t(\delta) = \sigma(\eta) = \bar{C}\eta$. This expression simplifies to $\delta = 0$ after having replaced η by its definition. We also note that $t(0) < \sigma_c$, where we define σ_c as $\bar{C}\delta_c$.

Case $\eta = \delta_c$

If $\eta = \delta_c$, then it is straightforward that $t(\delta) = \sigma_c - \sigma'(0)\delta$.

Therefore, we recover the classic linearly decreasing cohesive law by correcting the universal macroscopic cohesive law:

$$t(\delta) = \begin{cases} \sigma_c - \bar{C}\delta, & \text{if } \delta < \delta_c \\ 0, & \text{otherwise} \end{cases} \tag{A.4}$$

Bibliography

[1] T.L. Anderson. *Fracture Mechanics: fundamentals and applications.* CRC Press, Boca Raton, 1995.

[2] ASTMG47. *Standard test method for determining susceptibility to stress corrosion cracking of high strength aluminum alloy products*, volume 03.02, pages 173–177. ASTM, 1991.

[3] C. Atkinson and M.F. Kanninen. A simple representation of crack tip plasticity: the inclined strip-yield superdislocation model. *International Journal of Fracture*, 13:151–163, 1977.

[4] G. I. Barrenblatt. The mathematical theory of equilibrium of cracks in brittle fracture. *Advances in Applied Mechanics*, 7:55–129, 1962.

[5] O.H. Basquin. The exponential law of endurance tests. In *Proceedings of the American Society for Testing and Materials*, volume 10, pages 625–630, 1910.

[6] C.D. Beachem and B.F. Brown. A comparison of three precracked specimens for evaluating the susceptibility of high-strength streel to stress-corrosion cracking. Technical report, American Society for Testing and Materials, Philadelphia, 1967.

[7] B.A. Bilby and K.H. Swinden. Representation of plasticity at notches by linear dislocation arrays. *Proceedings of the Royal Society of London*, A285:22–33, 1965.

[8] A. Braides, G. Dal Maso, and A. Garroni. Variational formulation of softening phenomena in fracture mechanics, the one-dimensional case. *Archive for Rational Mechanics and Analysis*, 146(1):23–58, 1999.

[9] B.F. Brown. *Stress Corrosion Cracking Control Measures*, volume 156, chapter 1. National Bureau of Standards, 1977.

[10] B. Budiansky and J.W. Hutchinson. Analysis of closure in fatigue crack growth. *Journal of Applied Mechanics*, 45:267–276, 1978.

[11] G. T. Camacho. *Computational modelling of impact damage and penetration of brittle and ductile solids.* PhD thesis, Brown University, Providence, Rhode Island, May 1996.

[12] G. T. Camacho and M. Ortiz. Computational modelling of impact damage in brittle materials. *International Journal of Solids and Structures*, 33(20-22):2899–2938, 1996.

[13] L.F. Coffin. A study of the effect of cyclic thermal stress on a ductile metal. In *Transactions of the American Society of Mechanical Engineers*, volume 76, pages 931–950, 1954.

[14] A. M. Cuitiño and M. Ortiz. A material-independent method for extending stress update algorithms from small-strain plasticity to finite plasticity with multiplicative kinematics. *Engineering Computations*, 9:437–451, 1992.

[15] Y.F. Dafalias. *Modelling cyclic plasticity: simplicity versus sophistication*, pages 153–198. Wiley, New York, 1984.

[16] A. De-Andrés, J. L. Pérez, and M. Ortiz. Elastoplastic finite element analysis of three-dimensional fatigue crack growth in aluminum shafts subjected to axial loading. *International Journal of Solids and Structures*, 36(15):2231–2258, 1999.

[17] G. Del Piero and L. Truskinovsky. A one-dimensional model for localized and distributed failure. *Journal de Physique IV*, 8(P8):95–102, 1998.

[18] G. Del Piero and L. Truskinovsky. Macro- and micro-cracking in one-dimensional elasticity. *International Journal of Solids and Structures*, 38(6-7):1135–1148, 2001.

[19] R.J. Donahue, H.M. Clark, P. Atanmo, R. Kumble, and A.J. McEvily. Crack opening displacement and the rate of fatigue crack growth. *International Journal of Fracture Mechanics*, 8:209–219, 1972.

[20] D.C. Drucker and L. Palgen. On the stress-strain relations suitable for cyclic and other loading. *Journal of Applied Mechanics*, 48:479–485, 1981.

[21] D. S. Dugdale. Yielding of steel sheets containing slits. *Journal of the Mechanics and Physics of Solids*, 8:100–104, 1960.

[22] W. Elber. Fatigue crack closure under cyclic tension. *Engineering Fracture Mechanics*, 2:37–45, 1970.

[23] M.H. El Haddad, N.E. Dowling, T.H. Topper, and K.N. Smith. *J*-integral applications for short fatigue cracks at notches. *International Journal of Fracture*, 16:15–30, 1980.

[24] M.H. El Haddad, T.H. Topper, and K.N. Smith. Prediction of non-propagating cracks. *Engineering Fracture Mechanics*, 11:573–584, 1979.

[25] R.G. Foreman, V.E. Keary, and R.M. Engle. Numerical analysis of crack propagation in cyclic-loaded structures. *Journal of Basic Engineering*, 89:459–464, 1967.

[26] G.S. Frankel and R.M. Latanision. Hydrogen transport during deformation in nickel .1. polycrystalline nickel. *Metallurgical Transactions A-Physical Metallurgy and Materials Science*, 17(5):861–867, 1986.

[27] R.P. Gangloff. A review and analysis of the threshold for hydrogen environment embrittlement of steel. In Levy M. and Isserow S., editors, *Corrosion Prevention and Control*, pages 64 111, Watertown, MA, 1986. 33rd Sagamore Army Materials Research Conference, U.S. Army Laboratory Command.

[28] R.P. Gangloff. Crack tip modeling of hydrogen environment embrittlement - application to fracture-mechanics life prediction. *Materials Science and Engineering A-Structural Materials Properties Microstructure and Processing*, 103(1):157–166, 1988.

[29] H. Gerber. Bestimmung der zulässigen spannungen in eisen-konstructionen. *Zeitscrift des Bayerischen Architeckten und Ingenieur-Vereins*, 6:101–110, 1874.

[30] C.J. Gilbert, R.H. Dauskardt, and R.O. Ritchie. Microstructural mechanisms of cyclic fatigue-crack propagation in grain-bridging ceramics. *Ceramics International*, 23(5):413–418, 1997.

[31] C.J. Gilbert, R.N. Petrany, R.O. Ritchie, R.H Dauskardt, and R.W. Steinbrech. Cyclic fatigue in monolithic alumina: mechanisms for crack advance promoted by frictional wear of grain bridges. *Journal of Materials Science*, 30(3):643–654, 1995.

[32] N. Goldenfeld. *Lectures on Phase Transitions and the Renormalization Group.* Addison-Wesley, 1992.

[33] J. Goodman. *Mechanics Applied to Engineering.* Longmans Green, London, 1899.

[34] K. Gylltoft. A fracture mechanics model for fatigue in concrete. *Mater. Struct.*, 17:55–58, 1984.

[35] ASM International Handbook, editor. *Metals Handbook*, volume 19. tenth edition, 1990.

[36] ASM International Handbook, editor. *Metals Handbook*, volume 2. tenth edition, 1990.

[37] ASM International Handbook, editor. *Metals Handbook*, volume 1. tenth edition, 1990.

[38] D.A. Hordijk and H.W. Reinhardt. Growth of discrete cracks under fatigue loading. In S.P. Shah, editor, *Toughening mechanisms in quasi-brittle materials*, pages 541–554, Dordrecht, The Nederlands, 1991. Kluwer Academic Publishers.

[39] E.A.A. Jarvis, R.L. Hayes, and E.A. Carter. Effects of oxidation on the nanoscale mechanisms of crack formation in aluminum. *Chem. Phys. Chem.*, 2(1):55–59, 2001.

[40] M.F. Kanninen and C. Atkinson. Application of an inclined-strip-yield crack-tip plasticity model to predict constant amplitude fatigue crack growth. *International Journal of Fracture*, 16:53–69, 1980.

[41] M.F. Kanninen and C.H. Popelar. *Advanced Fracture Mechanics.* Oxford University Press, 1985.

[42] P. Kedzierzawski. In R.A Oriani, J.P. Hirth, and M. Smialowski, editors, *Hydrogen Degradation of Ferrous Alloys*, page 251, New Jersey, 1985. Noyes Publications.

[43] G.E. Kerns, M.T. Wang, and R.W. Staehle. In *Stress-Corrosion Cracking and Hydrogen Embrittlement of Iron-Based Alloys*, page 700, Houston, 1977. NACE, Staehle, R.W. and Hochmann J. and McCright R.D. and Slater J.E.

[44] M. Klesnil and P. Lukas. Influence of strength and stress history on growth and stabilization of fatigue cracks. *Engineering Fracture Mechanics*, 4:77–92, 1972.

[45] B. Ladna and H.K. Birnbaum. A study of hydrogen transport during plastic- deformation. *Acta Metallurgica*, 35(7):1775–1778, 1987.

[46] C. Laird. Mechanisms and theories of fatigue. In *Fatigue and Microstructure*, pages 149–203. American Society for Metals, 1979.

[47] B.N. Leis, M.F. Kanninen, A.T. Hopper, J. Ahmad, and D. Broek. A critical review of the short crack problem in fatigue. Technical report, Air Force Aeronautical Laboratories Report, May 1983.

[48] J. Lufrano and P. Sofronis. Enhanced hydrogen concentrations ahead of rounded notches and cracks - competition between plastic strain and hydrostatic stress. *Acta Materialia*, 46(5):1519–1526, 1998.

[49] S.S. Manson. Behavior of materials under conditions of thermal stress. Technical Report 1170, National Advisory Commission on Aeronautics, Lewis Flight Propulsion Laboratory, Cleveland, 1954.

[50] A.J. McEvily. On closure in fatigue crack growth. Technical report, American Society for Testing and Materials, Philadelphia, 1988.

[51] M.A. Miner. Cumulative damage in fatigue. *Journal of Applied Mechanics*, 12:159–164, 1945.

[52] N.R. Moody and A.W. Thompson, editors. *Hydrogen Effects on Material Behavior*, Warrendale, PA, 1990. TMS.

[53] J.D. Morrow. Fatigue design handbook—advances in engineering. In *Society of Automotive Engineers*, volume 4, pages 21–29, Warrendale, PA, 1968. Society of Automotive Engineers.

[54] A. Needleman. A continuum model for void nucleation by inclusion debonding. *Journal of Applied Mechanics*, 54:525–531, 1987.

[55] A. Needleman. An analysis of decohesion along an imperfect interface. *International Journal of Fracture*, 42(1):21–40, 1990.

[56] A. Needleman. An analysis of tensile decohesion along an interface. *Journal of the Mechanics and Physics of Solids*, 38(3):289–324, 1990.

[57] A. Needleman. Micromechanical modeling of interfacial decohesion. *Ultramicroscopy*, 40:203–214, 1992.

[58] H.G. Nelson and D.P. Williams. Quantitative observations of hydrogen induced slow crack growth in a low alloy steel. In Hochmann J., R.D. McCright, Slater J., and R.W. Staehle, editors, *Stress Corrosion Cracking and Hydrogen Embrittlement of Iron Based Alloys*, pages 390–404, Houston, TX, 1976. NACE.

[59] P. Neumann. The geometry of slip processes at a propagating fatigue crack. *Acta Metallurgica*, 22:1155–1178, 1974.

[60] R.C. Newman, K. Sieradzki, and H.S. Isaacs. Stress-corrosion cracking of sensitized type-304 stainless-steel in thiosulfate solutions. *Metallurgical Transactions A-Physical Metallurgy and Materials Science*, 13(11):2015–2026, 1982.

[61] M. Ortiz. Computational micromechanics. *Computational Mechanics*, 18(5):321–338, 1996.

[62] M. Ortiz and A. Pandolfi. Finite-deformation irreversible cohesive elements for three-dimensional crack-propagation analysis. *International Journal for Numerical Methods in Engineering*, 44(9):1267–1282, 1999.

[63] M. Ortiz and E.P. Popov. Accuracy and stability of integration algorithms for elastoplastic constitutive relations. *International Journal for Numerical Methods in Engineering*, 21(9):1561–1576, 1985.

[64] M. Ortiz and J.J. Quigley. Adaptive mesh refinement in strain localization problems. *Computer Methods in Applied Mechanics and Engineering*, 90(1-3):781–804, 1991.

[65] M. Ortiz and S. Suresh. Statistical properties of residual stresses and intergranular fracture in ceramic materials. *Journal of Applied Mechanics*, 60(1):77–84, 1993.

[66] Marcus P. and Oudar J., editors. *Stress-Corrosion Cracking*, chapter 10, page 311. Marcel Dekker, Inc., 270 Madison Avenue, New York, 1995.

[67] A. Palgren. Die lebensdauer von kugellagern. *Zeitschrift des Vereins Deutscher Ingenieure*, 68:339–341, 1924.

[68] A. Pandolfi and M. Ortiz. Solid modeling aspects of three-dimensional fragmentation. *Engineering with Computers*, 14(4):287–308, 1998.

[69] P.C. Paris, R.J. Bucci, E.T. Wessel, W.G.Jr. Clark, and T.R. Mager. An extensive study on low fatigue crack growth rates in a533 and a508 steels. Technical Report ASTM STP 513, American Society for Testing and Materials, Philadelphia, 1972.

[70] P.C. Paris and F. Erdogan. A critical analysis of crack propagation laws. *Journal of Basic Engineering*, 85:528–534, 1963.

[71] P.C. Paris, M.P. Gomez, and W.P. Anderson. A rational analytic theory of fatigue. *The trend in engineering*, 13:9–14, 1961.

[72] I. Part and E. Kaxiras. Ab-initio studies of hydrogen embrittlement in aluminum. To appear, 2001.

[73] Easterling K.E. Porter, A. *Phase transformations in Metals and Alloys*. Van Nostrand Reinhold, 1981.

[74] W. Prager. A new method of analyzing stress and strains in work-hardening plastic solids. *Journal of Applied Mechanics*, 23:493–496, 1956.

[75] G. Puglisi and L. Truskinovsky. Mechanics of a discrete chain with bi-stable elements. *Journal of the Mechanics and Physics of Solids*, 48(1):1–27, 2000.

[76] R. Radovitzky and M. Ortiz. Error estimation and adaptive meshing in strongly nonlinear dynamic problems. *Computer Methods in Applied Mechanics and Engineering*, 172(1-4):203–240, 1999.

[77] E. A. Repetto, R. Radovitzky, and M. Ortiz. Finite element simulation of dynamic fracture and fragmentation of glass rods. To appear in Computer Methods in Applied Mechanics and Engineering, 1999.

[78] J.R. Rice. Mechanics of crack-tip deformation and extension by fatigue. Technical report, American Society for Testing and Materials, Philadelphia, 1967.

[79] J.R. Rice and G.E. Beltz. The activation-energy for dislocation nucleation at a crack. *Journal of the Mechanics and Physics of Solids*, 42(2):333–360, 1994.

[80] J.R. Rice and J.S. Wang. Embrittlement of interfaces by solute segregation. *Materials Science and Engineering A-Structural Materials Properties Microstructure and Processing*, 107:23–40, 1989.

[81] J.H. Rose, J.R. Smith, and J. Ferrante. Universal features of bonding in metals. *Physical Review B-Condensed Matter*, 28(4):1835–1845, 1983.

[82] K. Sieradzki and R.C. Newman. Brittle behavior of ductile metals during stress-corrosion cracking. *Philosophical Magazine A-Physics of Condensed Matter Structure Defects and Mechanical Properties*, 51(1):95 132, 1985.

[83] K. Sieradzki and R.C. Newman. Stress-corrosion cracking. *Journal of Physics and Chemistry of Solids*, 48(11):1101–1113, 1987.

[84] J.C. Simo and T.A. Laursen. An augmented lagrangian treatment of contact problems involving friction. *Computers and Structures*, 42(1):97–116, 1992.

[85] M. Smialowski. In R.A. Oriani, J.P. Hirth, and M. Smialowski, editors, *Hydrogen Degradation of Ferrous Alloys*, page 561, New Jersey, 1985. Noyes Publications.

[86] C.R. Soderberg. Factor of safety and working stress. In *Transactions of the American Society of Mechanical Engineers*, volume 52, pages 13–28, 1939.

[87] P. Sofronis and R.M. Mcmeeking. Numerical-analysis of hydrogen transport near a blunting crack tip. *Journal of the Mechanics and Physics of Solids*, 37(3):317–350, 1989.

[88] E.A. Starke and J.C. Williams. Microstructure and the fracture mechanics of fatigue crack propagation. Technical report, American Society for Testing and Materials, Philadelphia, 1989.

[89] S. Suresh. *Fatigue of Materials*. Cambridge University Press, Cambridge, England, 1991.

[90] E.B. Tadmor, M. Ortiz, and R. Phillips. Quasicontinuum analysis of defects in solids. *Phil. Mag. A*, 73(6):1529–1563, 1996.

[91] V. Tvergaard and J. W. Hutchinson. Effect of strain dependent cohesive zone model on predictions of interface crack growth. *Journal de Physique IV*, 6(C6):165–172, 1996.

[92] D.H. Vermilyea. In *Stress-Corrosion Cracking and Hydrogen Embrittlement of Iron-Based Alloys*, page 208, Houston, 1977. NACE, Staehle, R.W. and Hochmann J. and McCright R.D. and Slater J.E.

[93] E.F.J. von Euw, R.W. Hertzberg, and R. Roberts. Delay effects in fatigue-crack propagation. Technical report, American Society for Testing and Materials, Philadelphia, 1972.

[94] J.S. Wang and H. Vehoff. The effect of the mobility of segregated atoms on interfacial embrittlement. *Scripta Metallurgica et Materialia*, 25(6):1339–1344, 1991.

[95] J. Weertman. Rate of growth of fatigue cracks calculated from the theory of infinitesimal dislocations distributed on a plane. *International Journal of Fracture Mechanics*, 2:460–467, 1966.

[96] O.E. Wheeler. Spectrum loading and crack growth. *Journal of Basic Engineering*, 94:181–186, 1972.

[97] J. Willenborg, R.M. Engle, and R.A. Wood. A crack growth retardation model using an effective stress concept. Technical Report AFFDL-TM-71-1-FBR, Air Force Flight Dynamics Laboratory Report, January 1971.

[98] A. Wöhler. Versuche über die festigkeit der eisenbahnwagenachsen. *Zeitscrift für Bauwesen*, 10, 1860. English Summary (1867). Engineering 4, 160–161.

[99] G. Xu, A.S. Argon, and M. Ortiz. Nucleation of dislocations from crack tips under mixed-modes of loading - implications for brittle against ductile behavior of crystals. *Philosophical Magazine A-Physics of Condensed Matter Structure Defects and Mechanical Properties*, 72(2):415–451, 1995.

[100] X. P. Xu and A. Needleman. Numerical simulations of fast crack growth in brittle solids. *Journal of the Mechanics and Physics of Solids*, 42(9):1397–1434, 1994.

[101] D.Z. Yankelevsky and H.W Reinhardt. Uniaxial behavior of concrete in cyclic tension. *Journal of Structural Engineering*, 115(1):166–182, 1989.

[102] H. Ziegler. A modification of prager's hardening rule. *Quarterly of Applied Mathematics*, 17:55–65, 1959.